



저작자표시-비영리-동일조건변경허락 2.0 대한민국

이용자는 아래의 조건을 따르는 경우에 한하여 자유롭게

- 이 저작물을 복제, 배포, 전송, 전시, 공연 및 방송할 수 있습니다.
- 이차적 저작물을 작성할 수 있습니다.

다음과 같은 조건을 따라야 합니다:



저작자표시. 귀하는 원저작자를 표시하여야 합니다.



비영리. 귀하는 이 저작물을 영리 목적으로 이용할 수 없습니다.



동일조건변경허락. 귀하가 이 저작물을 개작, 변형 또는 가공했을 경우에는, 이 저작물과 동일한 이용허락조건하에서만 배포할 수 있습니다.

- 귀하는, 이 저작물의 재이용이나 배포의 경우, 이 저작물에 적용된 이용허락조건을 명확하게 나타내어야 합니다.
- 저작권자로부터 별도의 허가를 받으면 이러한 조건들은 적용되지 않습니다.

저작권법에 따른 이용자의 권리는 위의 내용에 의하여 영향을 받지 않습니다.

이것은 [이용허락규약\(Legal Code\)](#)을 이해하기 쉽게 요약한 것입니다.

[Disclaimer](#)

공 학 박사 학 위 논 문

**Superfilling of submicron trenches by Co electrodeposition with
benzimidazole based single additive**

벤지이미다졸 기반 단일 첨가제에서의 코발트 전해 도금을 통한
서브마이크론 트렌치의 초등각 전착

2021년 2월

서울대학교 대학원

화학생물공학부

강 정 규

Superfilling of submicron trenches by Co electrodeposition with benzimidazole based single additive

벤지이미다졸 기반 단일 첨가제에서의 코발트 전해 도금을 통한

서브마이크론 트렌치의 초등각 전착

지도교수 김 재 정

이 논문을 공학박사 학위논문으로 제출함
2021 년 1 월

서울대학교 대학원
화학생물공학부
강 정 규

강정규의 공학박사 학위논문을 인준함
2021 년 1 월

위 원 장

김 영 규



부위원장

김 재 정



위 원

이 유 태



위 원

김 수 길



위 원

권 오 중



Abstract

Cobalt is one of the most promising materials to replace copper interconnect. In this study, submicron trenches were successfully filled without defect using benzene ring and imidazole based single additives as a suppressor and their filling mechanisms were investigated. Cobalt electrodeposition involves hydrogen evolution reaction (HER), and the proton supply in feature filling varies depending on the location because of the topographical characteristics, thereby resulting in electrode surface changes like pH and hydrogen adsorption. Based on this phenomenon, void-free trench filling was achieved using benzimidazole (BZI) as an additive, which has different suppression effects depending on pH. Linear sweep voltammetry experiments confirmed the modification in suppression behavior of the additive according to pH. Chronoamperometric transients were performed at a fixed BZI concentration to confirm the potential region, wherein actual cobalt deposition was suppressed. Chronoamperometric analysis with various rotation rates was also conducted to demonstrate the effect of proton concentration near the electrode on the suppression effect of BZI. Finally, a void-free filling working mechanism in a low aspect ratio trench using BZI was proposed. This study proposes, a single additive, whose

suppression behavior changes according to the change in pH of the electrode surface, by considering the pH of the cobalt deposition solution and pK_a value of the additive. Furthermore, it was demonstrated that void-free filling can be made even in a trench with a low aspect ratio by calculating the proton concentration distribution change during the filling process.

We also investigated the superconformal cobalt filling of submicron trenches by electrodeposition in the presence of 2-mercaptobenzimidazole (MBI), which suppresses both cobalt deposition and the HER. The mechanism through which this single additive enables superconformal cobalt filling is investigated. The formation and breakdown of the suppression layer are characterized by linear sweep voltammetry and chronoamperometry. The convection-driven local concentration of MBI exerts different suppressing effects on cobalt reduction and the HER, leading to a change in the deposition rate and the current efficiency of cobalt. These phenomena induce a deposition rate differential between the top and bottom of the submicron trench, enabling bottom-up cobalt filling with a V-shape profile. In this study, we introduced new additives for cobalt feature filling, which were previously introduced only a few, and explained each filling mechanism from the HER related perspective.

Keywords: submicron trench, cobalt, electrodeposition, single additive system, superfilling, hydrogen evolution reaction

Student number: 2017-38822

Content

Abstract.....	i
List of Tables.....	Vi
List of Figures.....	Vii
Chapter I. Introduction.....	1
1.1. Issues in interconnects and alternatives.....	1
1.2. Co electrodeposition and feature filling.....	7
1.3. Additives for the Co feature filling and the mechanism.....	12
1.4. Purpose of this study.....	15
Chapter 2. Experimental.....	17
2.1. Basic condition: electrolyte, additives, and electrode system.....	17
2.2. Electrochemical analysis and electrodeposition.....	20
Chapter III. Results and Discussion.....	23
3.1. Submicron trench filling using benzimidazole.....	23
3.1.1. Filling results of benzimidazole.....	26

3.1.2. Electrochemical behavior of benzimidazole.....	28
3.1.3. Filling mechanism of benzimidazole.....	37
3.2. Submicron trench filling using 2-mercaptobenzimidazole.....	45
3.2.1. Optimization of Co trench filling conditions.....	47
3.2.2. Effect of convection intensity on suppression strength.....	55
3.2.3. Filling mechanism of 2-mercaptobenzimidazole.....	62
Chapter IV. Conclusion.....	67
References.....	71
국문 초록.....	80

List of Tables

Table 1.1. Molecular structure and pK_a of benzimidazole derivatives.....	16
--	-----------

List of Figures

Figure 1.1.	Roadmap for logic devices (IRDS) (Ref. 1).....	4
Figure 1.2.	Cross-section image of Intel's 22-nm embedded DRAM stack (Ref.2).....	5
Figure 1.3.	Conductive metal area ratio according to line width (Ref. 9).....	6
Figure 1.4.	Schematic diagram of Co electrodeposition.....	10
Figure 1.5.	Three types of deposition profile during the feature filling: (a) subconformal, (b) conformal, (c) superconformal deposition.....	11
Figure 2.1.	Schematic diagram of the three-electrode system for the Co electrodeposition.....	19
Figure 3.1.	Structural change of BZI in solution at different pHs.....	24
Figure 3.2.	UV spectra obtained for benzimidazole at pH 2, 5.5, 6.5 and 10 at 25°C. Cobalt-free electrolyte used for UV absorbance consisted of 0.5 M H_3BO_3 and 1.0 M Na_2SO_4 . The pH was adjusted with H_2SO_4 and NaOH	25
Figure 3.3.	Cross sectional SEM images of 180 nm trenches deposited in an electrolyte consisting of 0.1 M $\text{CoSO}_4 \cdot 7\text{H}_2\text{O}$, 0.5 M H_3BO_3 and 1.0 M Na_2SO_4 (a-c) without and (d-f) with 100 μM BZI. Deposition was performed at (a,d) -1.0 V; (b,e) -1.05 V; (c,f) -1.1 V for 500 mC/cm^2 . The patterned substrates were rotating at 500 rpm.....	27
Figure 3.4.	Linear sweep voltammograms for Co deposition from the electrolyte consisting of 0.1 M $\text{CoSO}_4 \cdot 7\text{H}_2\text{O}$, 0.5 M H_3BO_3 and 1.0 M Na_2SO_4 with the addition of various BZI concentrations with (a) pH 3 and (b) pH 6. Experimental	

	currents are converted to current densities using the 0.071 cm^2 RDE area. The RDE was rotating at 500 rpm. Voltammetry was initiated at OCP with a 10 mV/s rate.....	32
Figure 3.5.	Linear sweep voltammograms with and without cobalt source at pH 3. Cobalt-free electrolyte consisted of $0.5 \text{ M H}_3\text{BO}_3$ and $1.0 \text{ M Na}_2\text{SO}_4$, and $0.1 \text{ M CoSO}_4 \cdot 7\text{H}_2\text{O}$ was added for the "with Co" case. Experimental currents are converted to current densities using the 0.071 cm^2 RDE area. The RDE was rotating at 500 rpm.....	33
Figure 3.6.	Current transients of Co deposition in (a) VMS and (b) VMS + $100 \text{ }\mu\text{M}$ BZI for various potentials at pH 3. Experimental currents are converted to current densities using the 0.071 cm^2 RDE area. The RDE was rotating at 500 rpm.....	34
Figure 3.7.	Current transients from the electrolyte $0.5 \text{ M H}_3\text{BO}_3$ and $1.0 \text{ M Na}_2\text{SO}_4$ with different rotation rate at pH 3. Experimental currents are converted to current densities using the 0.071 cm^2 RDE area.....	35
Figure 3.8.	Current transients of (a) VMS and (b) VMS + $100 \text{ }\mu\text{M}$ BZI with different rotation rate at pH 3. Experimental currents are converted to current densities using the 0.071 cm^2 RDE area.....	36
Figure 3.9.	Charge evolution of Co feature filling performed at -1.05 V in the (a) VMS and (b) VMS + $100 \text{ }\mu\text{M}$ BZI at pH 3. The patterned substrates were rotating at 500 rpm.....	41
Figure 3.10.	Proposed BZI working mechanism for void-free cobalt fill.....	42
Figure 3.11.	Cross section of a submicron trench.....	43

Figure 3.12. Dimensionless proton concentration vs. dimensionless distance below trench mouth.....	44
Figure 3.13. UV spectra obtained for 2-mercaptobenzimidazole at pH 2, 5.5, 6.5 and 10 at 25°C. Cobalt-free electrolyte used for UV absorbance consisted of 0.5 M H ₃ BO ₃ and 1.0 M Na ₂ SO ₄ . The pH was adjusted with H ₂ SO ₄ and NaOH.....	46
Figure 3.14. (a) Linear sweep voltammograms without cobalt source for HER. The electrolyte consisted of 0.5 M H ₃ BO ₃ and 1.0 M Na ₂ SO ₄ with the addition of various MBI concentrations at pH 3. (b) Linear sweep voltammograms for Co deposition in the VMS. Experimental currents are converted to current densities using the 0.071 cm ² RDE area. The RDE was rotating at 500 rpm. Voltammetry was initiated at OCP with a 10 mV/s rate.....	51
Figure 3.15. Cross sectional SEM images of 180 nm trenches deposited in the VMS with various MBI concentrations at pH 3. Deposition was performed at (a) -1.0 V, (b) -1.05 V (c) -1.1 V (d) -1.15 V vs Ag/AgCl for 300 mC/cm ² . The patterned substrates were rotating at 500 rpm.....	52
Figure 3.16. Cross sectional SEM images of 180 nm trenches deposited in the VMS without MBI at pH 3. Deposition was performed at -1.1 V vs Ag/AgCl for (a) 600 and (b) 800 mC/cm ² . The patterned substrates were rotating at 500 rpm.....	53
Figure 3.17. Current transients of Co deposition at (a) VMS and (b) VMS+150 µM MBI under various potentials. Experimental currents are converted to current densities using the 0.071 cm ² RDE area. The RDE was rotating at 500 rpm.....	54

- Figure 3.18.** Effect of rotation speed on the chronoamperometry for Co deposition at (a) VMS and (b) VMS+150 μM MBI. (c) Difference between the steady-state current density as a function of rotation speed. The base electrolyte consists of 0.1 M $\text{CoSO}_4 \cdot 7\text{H}_2\text{O}$, 0.5 M H_3BO_3 and 1.0 M Na_2SO_4 with pH 3. Chronoamperometry was performed at -1.1 V vs Ag/AgCl. Experimental currents are converted to current densities using the 0.071 cm^2 RDE area..... **59**
- Figure 3.19.** Comparison of Co film thickness as a function of rotation speed at MBI free and 150 μM MBI. The base electrolyte consists of 0.1 M $\text{CoSO}_4 \cdot 7\text{H}_2\text{O}$, 0.5 M H_3BO_3 and 1.0 M Na_2SO_4 with pH 3. The deposition was performed on the PVD Co wafer at -1.1 V vs Ag/AgCl for 1.0 C/cm^2 . The Co film thickness was measured by FE-SEM after cross section..... **60**
- Figure 3.20.** Comparison of cobalt film thickness simulating the conditions of top (150 μM MBI, 500 rpm) vs. bottom (50 μM MBI, 50 rpm). The base electrolyte consists of 0.1 M $\text{CoSO}_4 \cdot 7\text{H}_2\text{O}$, 0.5 M H_3BO_3 and 1.0 M Na_2SO_4 with pH 3. The deposition was performed on the PVD Co wafer at -1.1 V vs Ag/AgCl for 1.0 C/cm^2 . The cobalt film thickness was measured by FE-SEM after cross section..... **61**
- Figure 3.21.** The evolution of cobalt feature filling obtained at (a) -1.1 V and (b) -1.15 V in an electrolyte consisting of 0.1 M $\text{CoSO}_4 \cdot 7\text{H}_2\text{O}$, 0.5 M H_3BO_3 and 1.0 M Na_2SO_4 with 150 μM MBI at pH 3. The patterned substrates were rotating at 500 rpm..... **64**

Figure 3.22. The current transients curve during the trench-filling in the VMS with 150 μM of MBI at pH 3. Deposition was performed at -1.1 V vs Ag/AgCl for 400 mC/cm^2 . The patterned substrates were rotating at 500 rpm.....	65
Figure 3.23. Proposed MBI working mechanism for void-free cobalt fill under 500 rpm convection system. CE = current efficiency.....	66

CHAPTER I

Introduction

1.1. Issues in interconnects and alternatives

As technology advances, electronic devices are continuously scaled down and the dimensions of tungsten contacts or copper interconnects are inevitably reduced. This flow is illustrated in the road map for logic device as shown in Fig.1.1,¹ and will have the same direction in the memory device. In particular, the contact and M1/M2 have the narrowest width because they are located at the bottom of the electronic device, as shown in Fig. 1.2.² When the size of interconnect reduces below a certain level, resistivity, which is considered as an intrinsic characteristic of the material, increases rapidly because of the resistivity size effect.³⁻⁷ The size effect, which is the origin of the increase in resistivity, is related to the electron mean free path (EMFP). In general, in bulk materials, resistivity is dominated by electron–phonon scattering; therefore, the larger the EMFP, the lower the resistivity. However, as the line width of the interconnect approaches the EMFP, the surface collision and the grain boundary

scattering increases.^{7, 8} Therefore, the increase in resistivity of the conductive metal causes an increase in the resistance of interconnect. In addition, in contacts or interconnects, barrier layer such as Ti/TiN or Ta/TaN that prevents the diffusion of the conductive metal is used. Since the thickness of the barrier layer cannot be reduced below a certain value, the area for conductive metal decreases as the line width of the interconnect decreases as shown in Fig. 1.3.⁹ Therefore, as the line width decreases, the interconnect resistance increases rapidly. This phenomenon is evident at the interconnect line width of <10 nm, which was recently reported; moreover, line resistance increases to approximately 10 times that of bulk resistance.¹⁰ When the interconnect resistance increases, semiconductor power consumption increases and speed delay occurs, limiting the performance of the semiconductor device, and adversely affecting the continuous device scaling.¹¹ To overcome this limitation, it is advantageous to use a material that has a relatively small EMFP or maximize the volume of the conductive metal using a material capable of reducing or removing the barrier layer.^{12, 13} The candidate materials that satisfy these conditions are nickel, ruthenium, and cobalt. Among them, cobalt facilitates easy deposition and has a low cost, making it the most appropriate candidate.¹³ Also, cobalt has a much smaller EMFP of 11.8 nm compared to tungsten (15.5 nm) or copper (39.9 nm), and the barrier

layer can be reduced to 2 nm.^{14, 15} Due to these characteristics, cobalt has emerged as a suitable material to replace tungsten for contacts and copper for interconnects, and relevant research has been actively conducted.

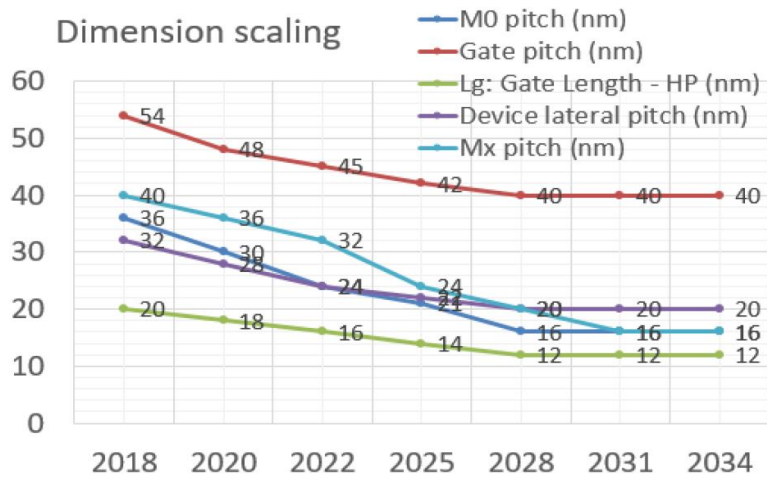


Figure 1.1. Roadmap for logic devices (IRDS) (Ref. 1).

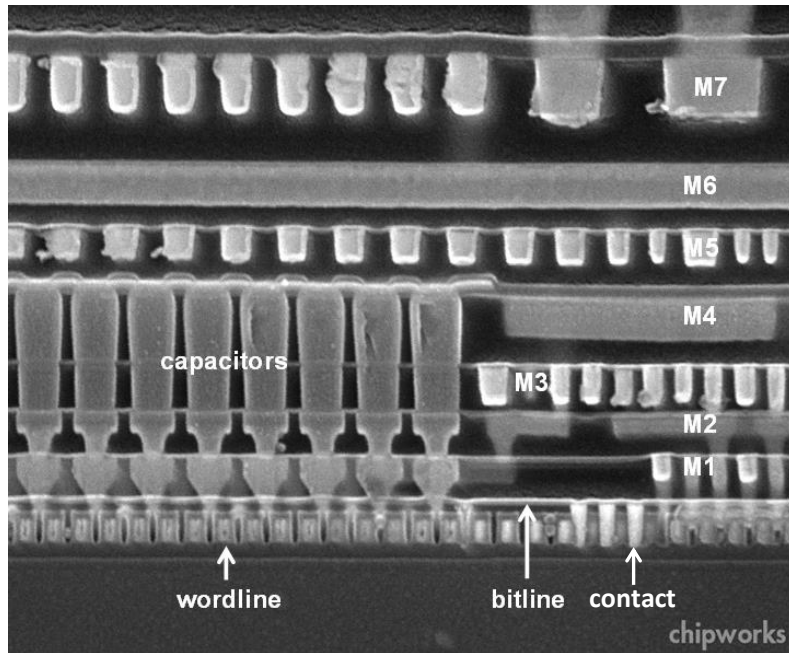


Figure 1.2. Cross-section image of Intel's 22-nm embedded DRAM stack (Ref.2).

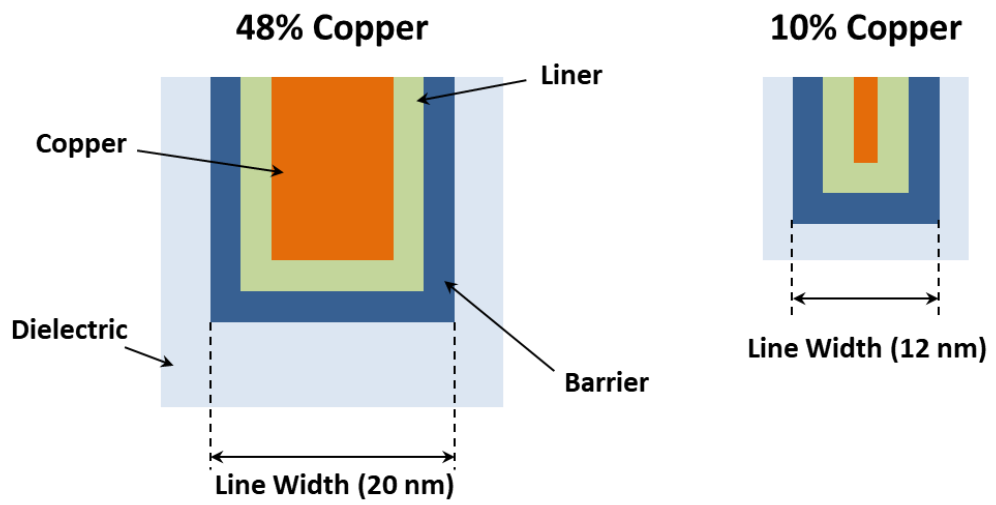
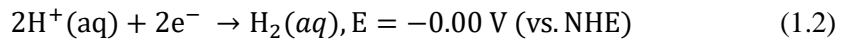
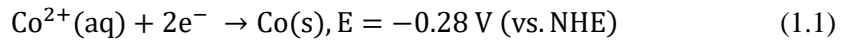


Figure 1.3. Conductive metal area ratio according to line width (Ref. 9).

1.2. Co electrodeposition and feature filling

Extensive studies have been reported on the application of cobalt in interconnects. Most of these studies focus on the resistance change and reliability after cobalt deposition through chemical vapor deposition (CVD).^{13, 16-23} Conversely, only a few studies on the metallization of cobalt interconnect formed by electrodeposition have been conducted although electrodeposition has various merits.²⁴⁻²⁷ Electrodeposition has a considerably shorter process time than CVD, and the deposition characteristics can be easily controlled by changing the applied current or voltage and by introducing additives. Cobalt electrodeposition is a process to reduce cobalt ions in the electrolyte on the conductive substrate by externally applying electrons as shown in Fig. 1.4. Cobalt electrodeposition occurs simultaneously with the hydrogen evolution reaction (HER), as can be seen from the standard reduction potentials in equations below.



As is well known, HER inevitably takes place during cobalt electrodeposition, and it is essential to become familiar with these secondary processes to understand cobalt electrodeposition. These secondary processes increase the pH at the electrode–electrolyte interface, and cobalt hydroxide may precipitate under the increased pH condition.^{28, 29} In this case, considerably large nodules and rough surfaces are formed and conductivity is reduced, resulting in a reduction in the quality of cobalt plating. To prevent this, boric acid with a buffering capability is mainly used in Watts-type plating baths.^{30, 31}

Cobalt has been used in the fields such as storage devices and magnetic sensors owing to its ferromagnetic nature. Therefore, previous researches on cobalt electrodeposition mainly focused on the cobalt structure, shape control, and deposition mechanism for the cobalt film on the plane substrate.³²⁻⁴⁸ In contrast, in patterned areas such as interconnects or contact, the purpose of the study is completely different. With the deposition conditions on the plane substrate, one cannot help obtaining subconformal or conformal deposition when performing feature filling. The subconformal and conformal deposition causes the formation of voids or seams as shown in Fig. 1.5. These defects expand during the repetitive operation of semiconductor devices after the annealing. To prevent the formation of voids or seams,

superconformal deposition, or so-called superfilling, is required for the device reliability. Superconformal filling can be achieved by selective deposition on the bottom of the feature, which induces bottom-up growth. In other word, for feature filling, a difference in deposition rate between the top and the bottom must be given, and for this purpose, the use of additives is essential. However, there are less than ten studies for cobalt feature filling, and further studies are needed.

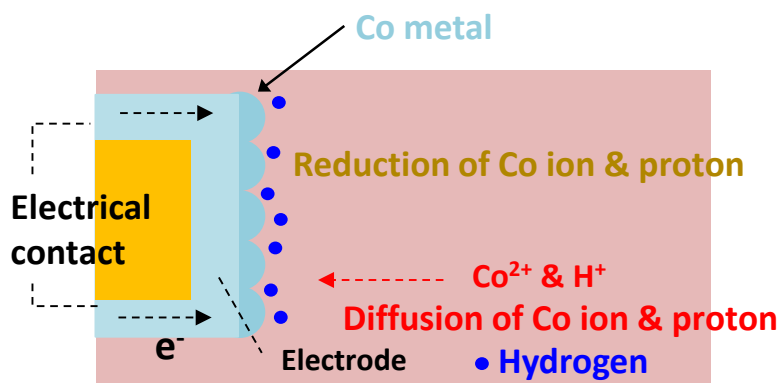


Figure 1.4. Schematic diagram of Co electrodeposition.

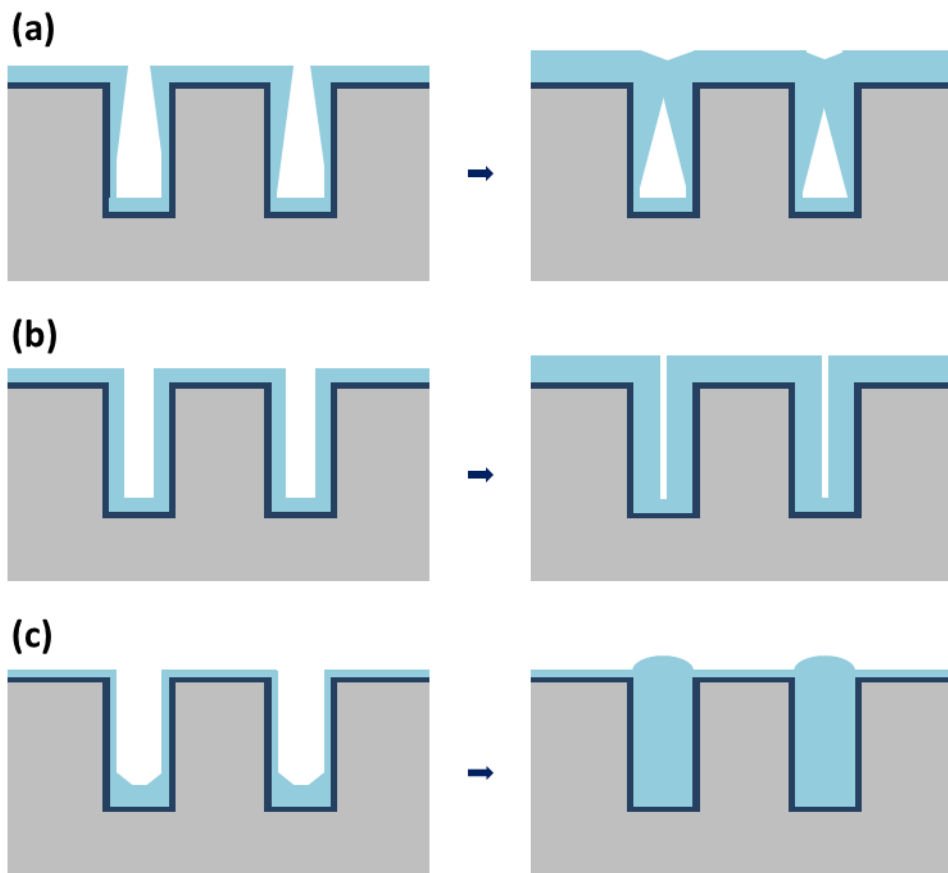


Figure 1.5. Three types of deposition profile during the feature filling: (a) subconformal, (b) conformal, (c) superconformal deposition.

1.3. Additives for the Co feature filling and the mechanism

Additives are widely used to modulate the conditions of plating in electrodeposition. In particular, when conducting feature filling, additives are essential components that cause a variation in the deposition speed depending on the deposition spots, thereby enabling the performance of superconformal growth. Copper bottom-up filling electrodeposition is carried out using a three-additive system consisting of a suppressor, an accelerator, and a leveler. Many studies have been conducted on the behavior of additives and their growth mechanisms; however, various additives are still being developed for copper electrodeposition.⁴⁹⁻⁵⁴ Conversely, for cobalt, most studies used a suppressor type of single additive. The use of a single additive simplifies the system and makes it easier to monitor the reliability of the solution. If superfilling is possible with only a single additive system, we may not have to use a multi additive system. There are studies on the additives and mechanisms for cobalt bottom-up filling with single additive system, although these are still insufficient. Some studies explain the mechanism based on the S-shaped negative differential resistance theory^{24, 25} and the deposition speed difference due to complex formation,⁵⁵ which has been suggested in copper bottom-up filling studies. Studies explaining the mechanisms based on the

interaction with the HER involved in cobalt reduction have also been reported.^{26, 27}

Proton reduction during cobalt electrodeposition causes a change in pH at the electrode surface.³¹ In addition, during the cobalt feature filling, the proton supply varies due to the difference in the convection rates at the top and bottom in spite of the high diffusion coefficient of proton, thereby affecting the pH depending on the location.⁵⁶⁻⁵⁸ Therefore, the use of additives whose suppression effect changes in accordance with pH would manipulate the bottom-up filling characteristics.^{26, 59} Similarly, if an additive that can suppress the HER in the potential region of cobalt deposition is used, the current efficiency can be increased, and the quality of the plating can be improved by inhibiting the increase in pH.

Since cobalt is included in the iron group metal, it was referred to in the selection of additives for feature filling through various studies which introduce new additives for electrodeposition with iron group metals.^{25, 60-70} In the case of nickel, one of the iron group metals, there have also been many studies on additives for superconformal filling. Polyethyleneimine (PEI) and benzimidazole derivatives, such as 2-mercaptobenzimidazole (MBI) and 2-mercapto-5-benzimidazolesulfonic acid (MBIS), were shown to yield void-free feature filling.^{64, 66-70} A common feature of these additives is that they contain a benzene ring or nitrogen atom. The benzene ring

maintains the adsorption through the interaction of π -electrons with substrate. In addition, the nitrogen atom achieves effective adsorption by donating the unshared electrons to the substrate. Benzimidazole derivatives mainly consist of the fusion of benzene ring and imidazole as shown in Table 1.1. Therefore, we considered benzimidazole derivatives as a single additive for cobalt superconformal electrodeposition. Among the benzimidazole derivatives, 2-mercaptobenzimidazole-5-sulphonic acid, which has been already studied,²⁵ and benzotirazole, which cannot give a difference in top-bottom deposition rate by forming a web-shaped inhibitory layer⁷¹ are excluded. 2-Mercaptobenzimidazole and benzimidazole have not yet been introduced for cobalt superfilling, and they are expected to exhibit effective suppression on cobalt deposition. Therefore, we selected these two materials and studied to apply them to cobalt superfilling.

1.4. Purpose of this study

It is obvious that additives have a critical role in bottom-up feature filling with the relatively strong suppression on the top accompanying the weak or no suppression on the bottom. Also, in cobalt electrodeposition, the relationship between additives and HER should be investigated in depth. In this study, new kinds of additives are introduced based on the molecular structures of additives reported previously. Benzimidazole (BZI) and 2-mercaptobenzimidazole (MBI) were introduced as additive which has cobalt deposition suppressing effect. By adding the suppressors, void-free superconformal filling was achieved. However, the filling profile was markedly different. Therefore, we tried to understand the working mechanism of both additives, respectively.

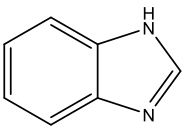
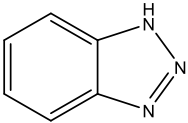
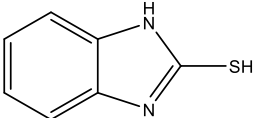
Additive	Structure	pK_{a1}	pK_{a2}
Benzimidazole		5.6	12.8
Benzotriazole		< 0	8.2
2-Mercaptobenzimidazole		< 0	10.4

Table 1.1. Molecular structure and pK_a of benzimidazole derivatives.

CHAPTER II

Experimental

2.1. Basic condition: electrolyte and electrode system

The electrochemical measurements and trench filling experiments were performed in a three-electrode system with a potentiostat (PAR 273A, Princeton Applied Research) as shown in Fig. 2.1. A Co rotating-disk electrode (RDE, 0.071 cm^2) and Cu seeded submicron trench wafer were used as working electrode for purpose of each experiments. The width and height of the feature were 180 and 360 nm, respectively, thus aspect ratio (height/width) was 2. A Pt mesh and Ag/AgCl electrode (KCl saturated) were used as the counter and reference electrodes, respectively. The virgin makeup solution (VMS) for cobalt electrodeposition consisted of 0.1 M $\text{CoSO}_4 \cdot 7\text{H}_2\text{O}$, 0.5 M H_3BO_3 , and 1.0 M Na_2SO_4 , and the pH was adjusted to 3 by adding H_2SO_4 . Since boric acid has buffering capability, it prevents cobalt hydroxide precipitation due to hydrogen evolution.⁷² The 0.5 M of boric acid was added because the buffering ability was saturated above that concentration. Sodium sulfate was used as a supporting

electrolyte because it does not participate in electrochemical reactions and to improve electrolyte's conductivity.⁷³ In order to lower the solution resistance to the minimum, sodium sulfate was added to the maximum that can be dissolved. The temperature of the electrolytes was precisely controlled at 25 °C. The rotation rate is 500 rpm during electrodeposition unless otherwise specified. UV spectra for additives were obtained and analyzed using a UV-VIS spectrometer (Genesys-10, Thermo). BZI or MBI (50 μ M) were dissolved in deionized (DI) water and pH was adjusted using H₂SO₄ and NaOH. Each sample was analyzed in a 10 mm-length quartz cuvette using wavelengths in the region of 200–900 nm against the DI blank.

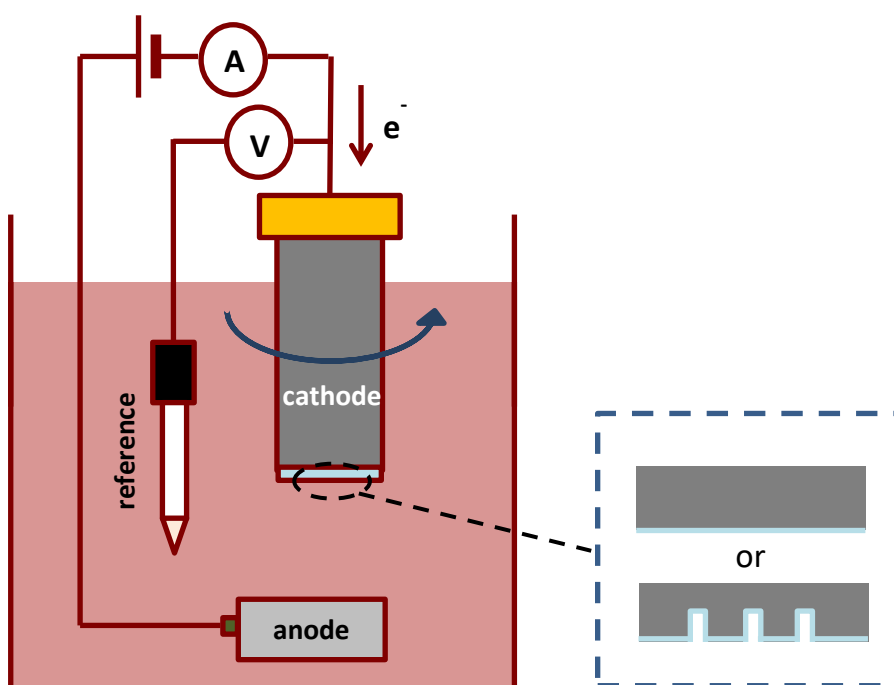


Figure. 2.1. Schematic diagram of the three-electrode system for the Co electrodeposition.

2.2. Electrochemical analysis and electrodeposition

The electroanalytical measurements and electrodeposition were performed with a potentiostat (PAR 273A, Princeton Applied Research) in a three-electrode system, including a working electrode, with Pt mesh and Ag/AgCl electrode (KCl saturated) as the counter and reference electrodes, respectively. The temperature of the electrolytes was maintained at 25 °C using a thermostat.

Four different concentrations of BZI (25, 50, 100, and 200 μM) and MBI (50, 100, 150, and 200 μM) were added to the electrolytes to investigate their effect on cobalt deposition. The electrochemical behavior of BZI and MBI was investigated by linear sweep voltammetry (LSV) and chronoamperometric transients using a cobalt RDE with a geometric area of 0.071 cm^2 as the working electrode. Cobalt rod (Avention®, 3 mm diameter and 99.9 % metal basis) was inserted into Teflon holder (12 mm diameter) for usage as the electrode for the RDE system. The surface of the cobalt RDE was polished using a 2000-grit sand paper after which it was rinsed with deionized (DI) water and blown dry with N_2 prior to the electrochemical analyses. The voltammetric response was scanned from OCP to -1.4 V (vs. Ag/AgCl) at a scan rate of 10 mV/s and rotating rate of 500 rpm for the RDE to overcome the diffusional limitation of cobalt

ion. Chronoamperometric experiments were performed by immersing the specimens under open circuit conditions, and after a few seconds the potential was stepped to initiate cobalt deposition.

The submicron trench filling was performed with a trench-patterned Si wafer supplied by SK Hynix, Inc. with a width of 180 nm and a depth of 360 nm. The substrates were metalized by the physical vapor deposition (PVD) of a Ta barrier layer and a copper seed layer. Prior to electrodeposition, a coupon wafer, fragmented at $1.5\text{ cm} \times 1.5\text{ cm}$, was loaded on the Teflon holder to expose an area of 1 cm^2 . Before the electrodeposition of the cobalt seed layer, the wafer was immersed into an aqueous solution of 0.03 M citric acid and 0.034 M potassium hydroxide for 2 min to remove the native oxide of copper. Cobalt was electrochemically deposited onto the oxide-etched coupon wafer at a potential of -1.0 V , with a deposition charge of 10 mC/cm^2 . The substrate was rotated at 500 rpm to apply convection during the filling process. Cross-sectional images were obtained using field emission scanning electron microscopy (FESEM, S-4800, Hitachi) to investigate the trench filling performance.

The comparison of the cobalt film thickness as a function of the rotation speed was performed on planar Si substrates covered with a PVD Ti/TiN barrier layer and a PVD cobalt layer. The cobalt film deposition was examined by chronoamperometry on a 1

cm² area. The cobalt film thickness was evaluated from the cleaved cross-sections in the FESEM.

Results and Discussion

3.1. Submicron trench filling using benzimidazole

Considering the increase in pH at the electrode surface by proton reduction, a pK_a value slightly larger than the pH value of a typical cobalt deposition solution (pH 2.5–4.5) is required.^{24, 25, 27, 55, 59} Therefore, we selected BZI as an additive to match these properties. Since pK_{a1} of BZI is 5.6 as shown in Table 1.1, it would exist mostly in the protonated form at a low pH; however, if the pH is increased in the vicinity of the electrode, the proportion of the neutral form would increase (Fig. 3.1). Ultraviolet (UV) spectra shows that the BZI molecule changes with pH, as shown in Fig. 3.2. The difference in the electron distribution between the uncharged benzimidazole and relevant benzimidazolium ion in acidic medium is responsible for the shifts in the absorption spectra from 265 nm to 269 nm.⁷⁴ Herein, the change in suppression behavior of BZI according to the concentration of protons was analyzed and applied to trench filling.

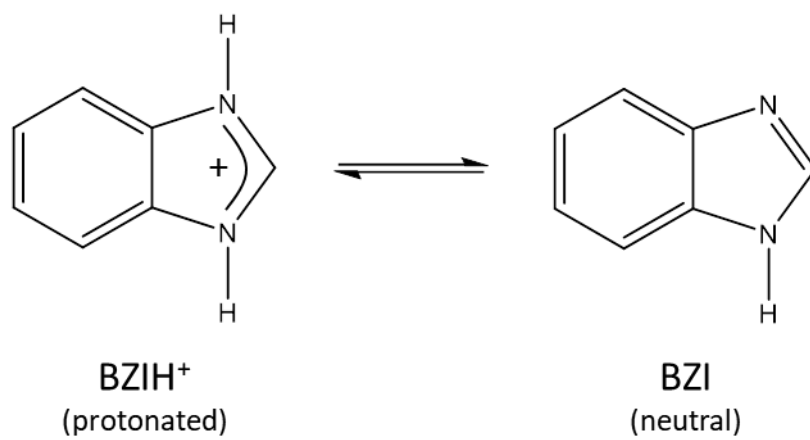


Figure 3.1. Structural change of BZI in solution at different pHs.

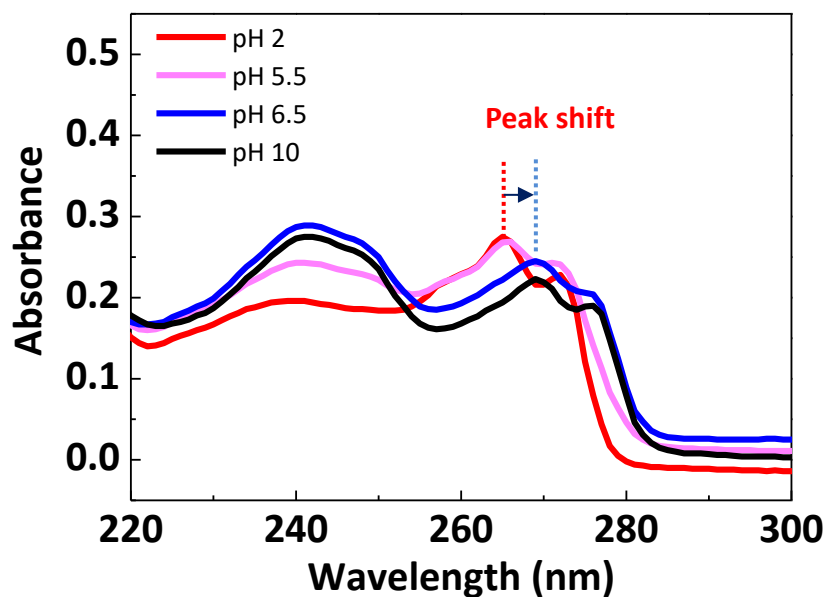


Figure 3.2. UV spectra obtained for benzimidazole at pH 2, 5.5, 6.5 and 10 at 25°C. Cobalt-free electrolyte used for UV absorbance consisted of 0.5 M H_3BO_3 and 1.0 M Na_2SO_4 . The pH was adjusted with H_2SO_4 and NaOH .

3.1.1. Filling results of benzimidazole

The influence of BZI on cobalt trench filling was examined by chronoamperometric electrodeposition. For reference purposes, the cobalt deposition in the absence of BZI is shown in Figs. 3.3a–3c. It was observed that voids were formed at the center of the trench, as cobalt was deposited conformally under all potential conditions. When a potential of -1.0 V was applied in the presence of $100\text{ }\mu\text{M}$ BZI, it can be inferred that BZI acted as a suppressor because cobalt deposition was suppressed, and only the seed layer was exposed, as shown in Fig. 3.3d. When potentials of -1.05 and -1.1 V were applied, complete void-free filling was obtained. We investigated the reasons for void-free filling with BZI throughout this study.

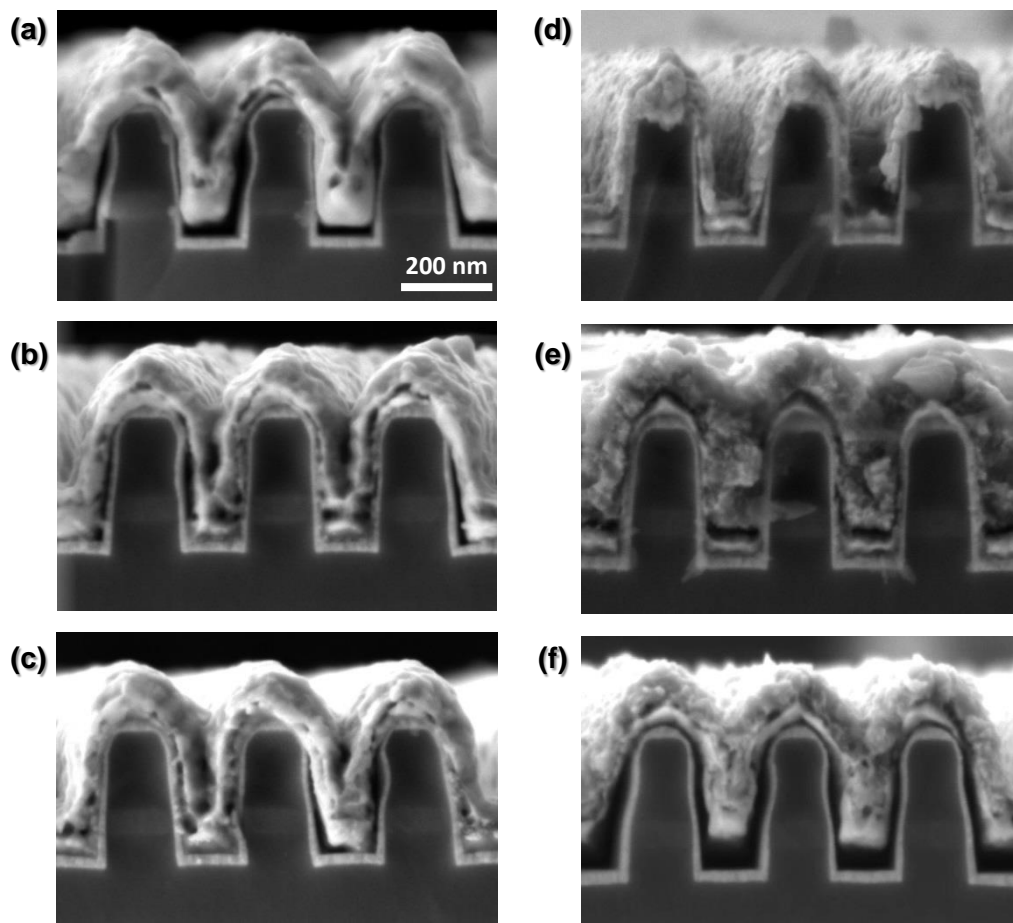


Figure 3.3. Cross sectional SEM images of 180 nm trenches deposited in an electrolyte consisting of 0.1 M $\text{CoSO}_4 \cdot 7\text{H}_2\text{O}$, 0.5 M H_3BO_3 and 1.0 M Na_2SO_4 (a-c) without and (d-f) with 100 μM BZI. Deposition was performed at (a,d) -1.0 V; (b,e) -1.05 V; (c,f) -1.1 V for 500 mC/cm^2 . The patterned substrates were rotating at 500 rpm.

3.1.2. Electrochemical behavior of benzimidazole

The LSV curves obtained on cobalt RDE with different amounts of BZI at pH of 3 and 6 are shown in Fig. 3.4. The potential was swept from OCP to -1.4 V with a sweep rate of 10 mV/s. First, we investigated the LSV behavior at pH 3 (Fig. 3.4a). When BZI was absent in the solution, the cathodic deposition current density started at -0.86 V, whereas hydrogen evolution started to occur at -0.48 V as shown in Fig. 3.5. When BZI was added up to 50 μ M, there was no significant change in current density behavior. However, when BZI present in the solution was 100 μ M, the deposition was significantly polarized in the low current range. The onset of the cobalt reduction shifted to -1.08 V. At a potential more negative than -1.08 V, the breakdown of the suppression layer caused the rapid acceleration of the cobalt deposition rate. Increasing the concentration of BZI to 200 μ M caused a stronger suppression of the cathodic current density; however, the onset potential for cobalt deposition was not significantly shifted from that of 100 μ M BZI. Therefore, after the suppression layer is formed at a certain concentration, the onset potential of the cobalt deposition is not significantly affected by the additive concentration. To determine whether the structural change of

BZI according to pH affects the suppression ability, the pH of the solution was increased from 3 to 6 to make BZI neutral form. Subsequently, LSV experiments were conducted with different amounts of BZI at a pH of 6, as shown in Fig. 3.4b. There was no significant change in current density compared to that without BZI, even at 200 μM BZI. This suggests that BZI does not have a suppression effect in the neutral form, whereas in the protonated form it has a suppression effect.

In addition to LSV, chronoamperometric transients for cobalt deposition were conducted on cobalt RDE. The transient currents for cobalt deposition obtained at different applied potentials are shown in Fig. 3.6a and 3.6b. For values more negative than -0.9 V, hydrogen evolution and cobalt deposition occurred simultaneously in the VMS. Therefore, the current density increases as the potential becomes more negative, as shown in Fig. 3.6a. However, when 100 μM BZI was used, only hydrogen evolution current was detected over a potential range of -0.9 to -0.95 V (Fig. 3.6b). For potentials more negative than -1.0 V, the formation of the suppression layer was significant and consequently the current density increased. In contrast to the case where BZI was not added, the current density was lower approximately in the range of $3\text{--}4$ mA/cm^2 ; therefore, there was a suppression effect, but not significant enough to completely suppress the cobalt deposition.

In acidic conditions, at a pH of 3, most of the BZI would be in the protonated form.⁷⁵ If the pH increases due to the hydrogen evolution reaction on the electrode surface and protons are insufficiently supplied, the suppression could be weakened due to changes in the molecular form of BZI. To confirm this, the rotation rate was changed to provide a difference in convection. Usually, it can be thought that the mobility of protons is very fast and will not be affected by mass transfer; however, the proton concentration at the electrode surface is affected by convection, as the current density changes according to the rotation rate.^{56, 57} To confirm that even though the diffusion coefficient of proton is very high, the supply of proton is also affected by the convection strength, the current density changes with rpm was observed in the solution without cobalt source as shown in Fig. 3.7.

To investigate the effect of convection both on BZI and cobalt electrodeposition, a potential of -0.95 V was selected and the rotation rate was changed. In case of VMS (Fig. 3.8a), the current density increased due to an enhanced supply of cobalt precursors and protons as the rotation rate increased. Alternatively, the addition of BZI (Fig. 3.8b) shows a significant difference with the VMS. At 400 and 500 rpm, where the rotation rate is relatively high, the pH is kept low because of the sufficient supply of protons. It maintains a significant suppression of cobalt deposition, resulting in a

low current density. However, the cobalt deposition was accelerated from 300 rpm, and the suppression strengths were clearly weakened at 200 and 100 rpm. As the convection strength decreases, the proton supply to the electrode surface also decreases, thereby increasing the pH of the electrode surface; therefore, a portion of BZI is changed from the protonated to neutral form. This property may account for the bottom-up filling in the feature. The suppression of cobalt deposition is maintained at the top, where the pH is kept low due to strong convection. However, at the bottom where the proton supply is not sufficient due to low convection, BZI turns into the neutral form, weakening the suppression strength and allowing for the bottom-up filling.

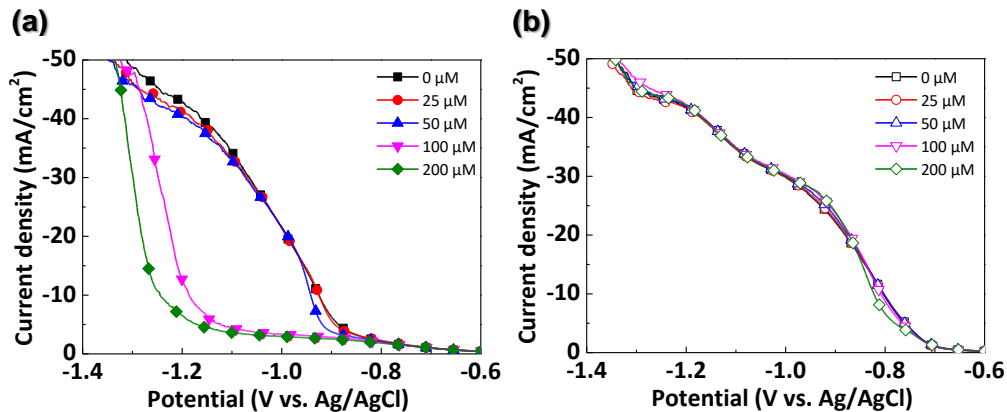


Figure 3.4. Linear sweep voltammograms for Co deposition from the electrolyte consisting of 0.1 M $\text{CoSO}_4 \cdot 7\text{H}_2\text{O}$, 0.5 M H_3BO_3 and 1.0 M Na_2SO_4 with the addition of various BZI concentrations with (a) pH 3 and (b) pH 6. Experimental currents are converted to current densities using the 0.071 cm^2 RDE area. The RDE was rotating at 500 rpm. Voltammetry was initiated at OCP with a 10 mV/s rate.

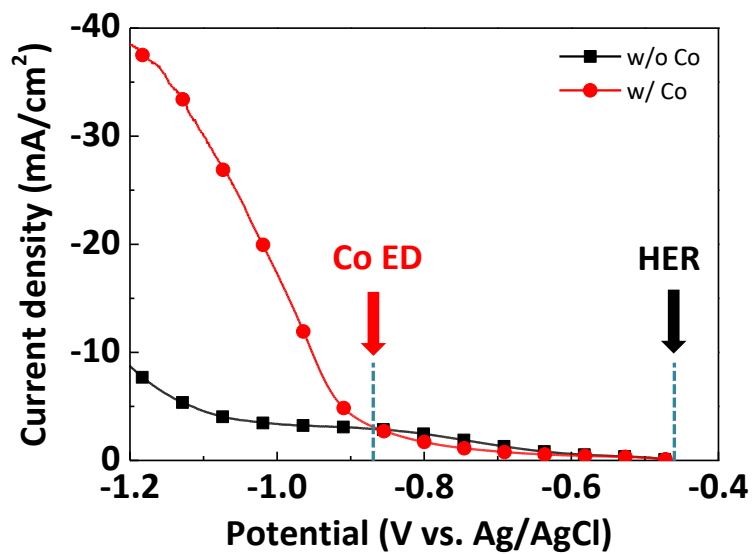


Figure 3.5. Linear sweep voltammograms with and without cobalt source at pH 3.

Cobalt-free electrolyte consisted of 0.5 M H_3BO_3 and 1.0 M Na_2SO_4 , and 0.1 M $\text{CoSO}_4 \cdot 7\text{H}_2\text{O}$ was added for the "with Co" case. Experimental currents are converted to current densities using the 0.071 cm^2 RDE area. The RDE was rotating at 500 rpm.

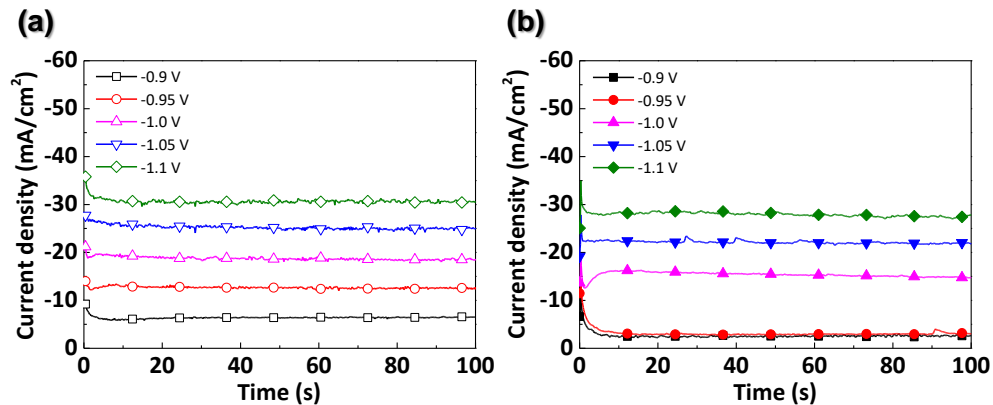


Figure 3.6. Current transients of Co deposition in (a) VMS and (b) VMS + 100 μM BZI for various potentials at pH 3. Experimental currents are converted to current densities using the 0.071 cm^2 RDE area. The RDE was rotating at 500 rpm.

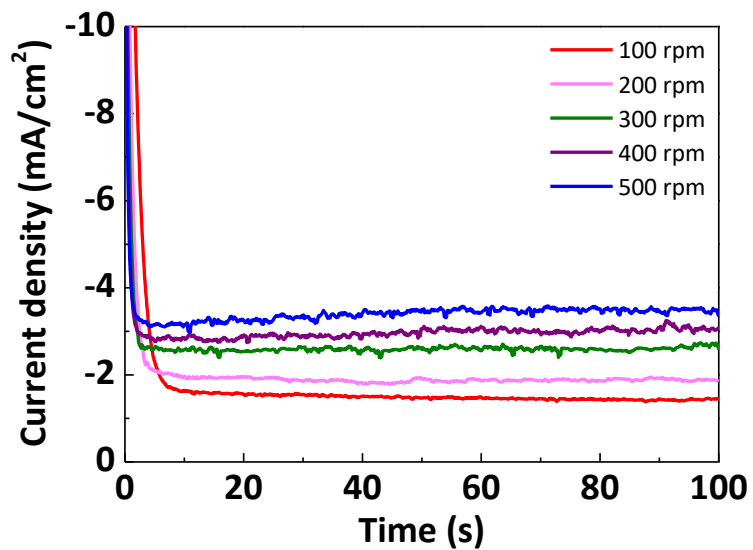


Figure 3.7. Current transients from the electrolyte 0.5 M H_3BO_3 and 1.0 M Na_2SO_4 with different rotation rate at pH 3. Experimental currents are converted to current densities using the 0.071 cm^2 RDE area.

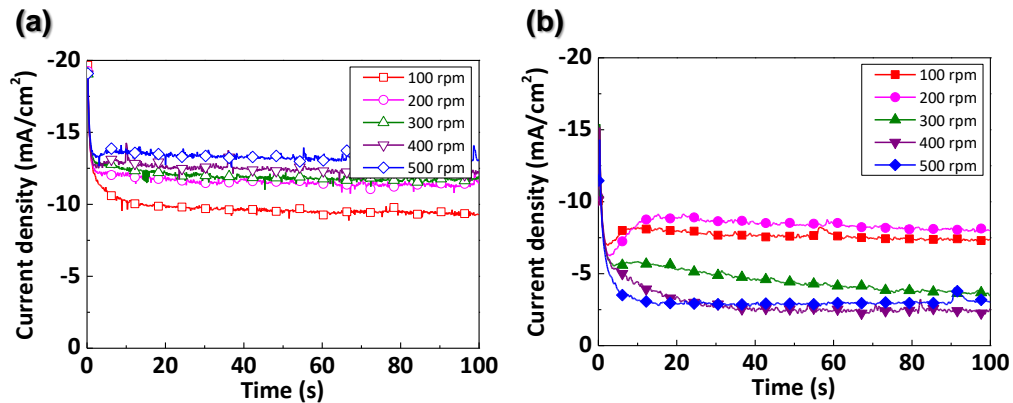


Figure 3.8. Current transients of (a) VMS and (b) VMS + 100 μM BZI with different rotation rate at pH 3. Experimental currents are converted to current densities using the 0.071 cm^2 RDE area.

3.1.3. Filling mechanism of benzimidazole

The shape evolution observed during trench filling by sectioning a series of specimens as a function of deposition charge is shown in Fig. 3.9. The specimens were electrodeposited at -1.05 V with $100\text{ }\mu\text{M}$ of BZI, where superconformal filling was achieved (Fig. 3.3). Initially, growth proceeded conformally in both the absence and presence of $100\text{ }\mu\text{M}$ BZI. Additional charges lead to the formation of voids in the case of the VMS with conformal deposition. However, when BZI was added, the gap in the center of the trench was quickly filled. In cobalt electrodeposition, the current efficiency decreases as the current density decreases.^{26, 59} Therefore, when BZI is added, both the current density and current efficiency are lower than that of VMS. This means that when the same charge was applied, since a smaller amount of charge was used for cobalt deposition, the total amount of deposited cobalt was also small. Nevertheless, when BZI was used, the trench was filled faster than the VMS case, and demonstrating that the partial current density applied to the bottom side of the trench was greater than that at the top. For VMS, the current density was applied equally at the top and bottom, and the conformal deposition was maintained until void was formed.

Figure 3.10 shows the proposed scheme for void-free cobalt fill in the presence of BZI. Even though the trench has the low aspect ratio of 2 as shown in Fig. 3.9, the difference in convection strength between the top and bottom is significant.⁷⁶⁻⁷⁸ However, cobalt deposition proceeds at almost the same deposition rate regardless of the location. This means that the pH gradient was not sufficiently generated inside the trench because of the high diffusion coefficient of proton. However, as deposition progresses, the aspect ratio of the central space of the trench gradually increases. This makes the proton supply more retarded and pH gradients develop within the trench. In order to show that the proton concentration gradient occurs inside the trench, we referred to a study in which Takahashi calculated the copper ion concentration according to the depth in the submicron trench.⁷⁸

A Peclet number can be calculated by a following equation.

$$Pe = \frac{0.51\omega^{\frac{3}{2}}\nu^{-\frac{1}{2}} \times \bar{r} \times 3.6 \left(\frac{\nu}{\omega}\right)^{\frac{1}{2}} \times \omega}{D_{H^+}} = 0.0237$$

\bar{r} is the wafer radius (cm), ω is the rotation rate (s^{-1}), and ν is the kinematic viscosity (cm^2/s). D_{H^+} is the diffusion coefficient of the proton. The Peclet number is 0.0237, even at the trench mouth, so convection is not important and diffusion controls the mass transport in submicron trenches. In the 1D model, the characteristic length is

L and the width is w (Fig. 3.11). By using Eq. 3.1 (Eq. 10 in Ref. 78), the transport material was replaced from copper ion to proton, and the dimensionless diffusion parameter ξ_D was calculated.

$$\frac{\partial^2 C^*}{\partial y^{*2}} = \frac{2i_{l,0}L^2}{C_0D_{H^+}wnF} C^* = \xi_D C^* \quad (3.1)$$

C^* is the proton concentration at y divided by the proton concentration in the bulk solution. y^* is the distance from top divided by L . Boundary conditions are $C^* = 1$ at $y^* = 0$, and $dC^*/dy^* = 0$ at $y^* = 1$. $C_0 = 10^{-3}$ mol L⁻¹, $D_{H^+} = 9.311 \times 10^{-5}$ cm² s⁻¹ (from CRC Handbook), $n = 1$, $F = 96,485 \times 10^3$ mC mol⁻¹ and $i_{l,0} = 4$ mA/cm². Exact solution to Eq. 3.1 was derived and given in Eq. 3.2

$$C^* = \frac{e^{d(2-y^*)} + e^{dy^*}}{e^{2d} + 1} \quad (3.2)$$

where $d = (\xi_D)^{1/2}$.

The concentration profile of proton was illustrated using Eq. 3.2 and shown in Fig. 3.12. When the aspect ratio is small, there is almost no difference in proton concentration at the top and bottom. As the trench sidewall grows out toward the center line, however, the trench width decreases and aspect ratio increases, eventually leading to formation of substantial proton concentration gradient. Then, as the proportion of

neutral BZI increases at the bottom, the suppression effect disappears, which causes a difference in the deposition rate between the top and bottom. In this way, in the feature with a low aspect ratio, conformal deposition is initially performed, but a difference in deposition rate occurs as the aspect ratio changes during the deposition process, and spontaneous void-free filling is achieved. Furthermore, because the diffusion coefficient of BZI is lower than that of proton, a concentration gradient would be naturally formed. Then, the BZI concentration at the bottom is lowered, which gives a synergetic effect on the bottom-up filling.

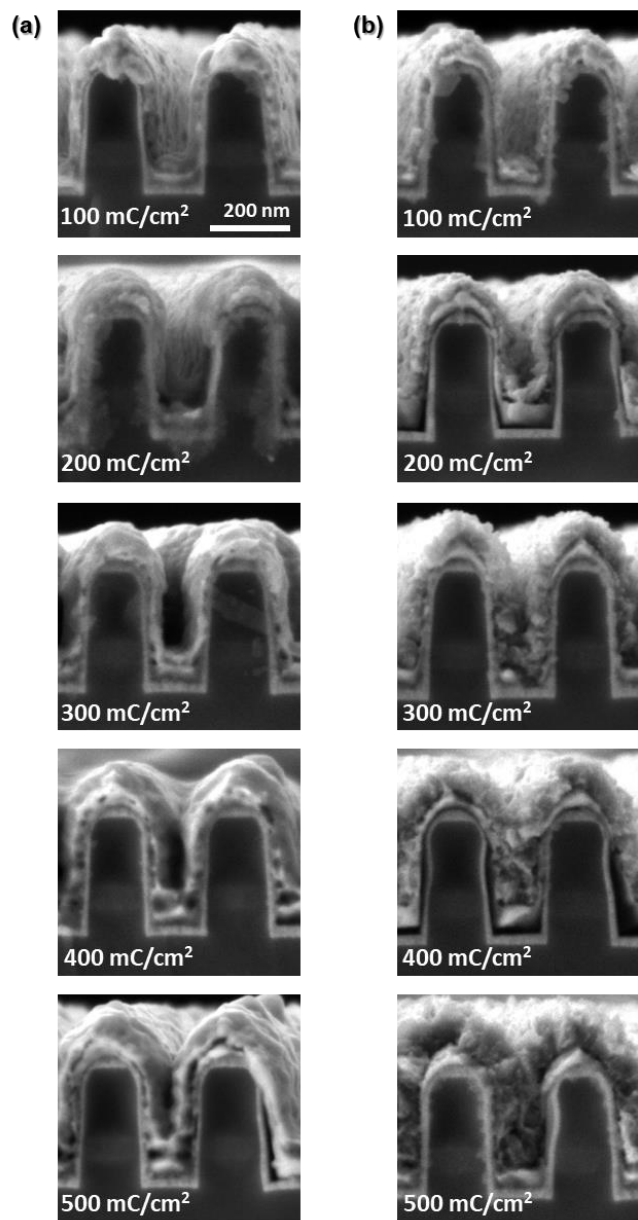


Figure 3.9. Charge evolution of Co feature filling performed at -1.05 V in the (a) VMS and (b) VMS + $100\ \mu\text{M}$ BZI at pH 3. The patterned substrates were rotating at 500 rpm.

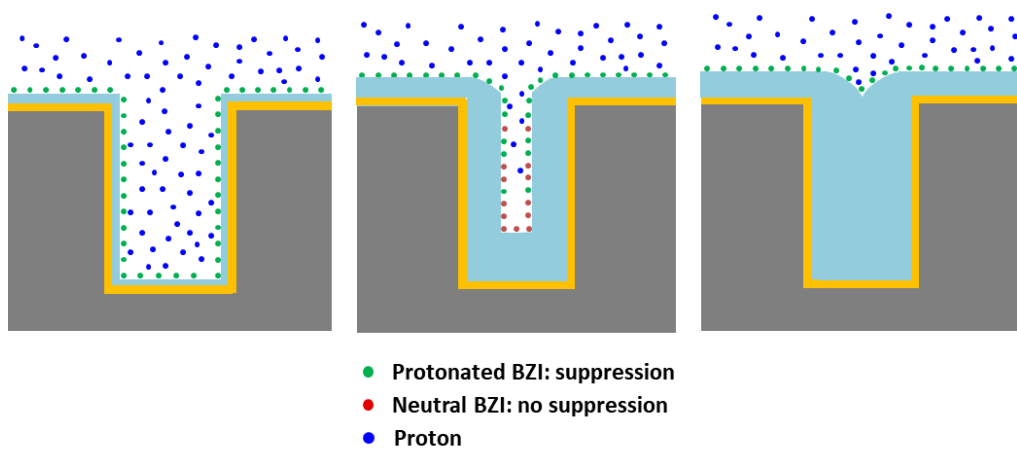


Figure 3.10. Proposed BZI working mechanism for void-free cobalt fill.

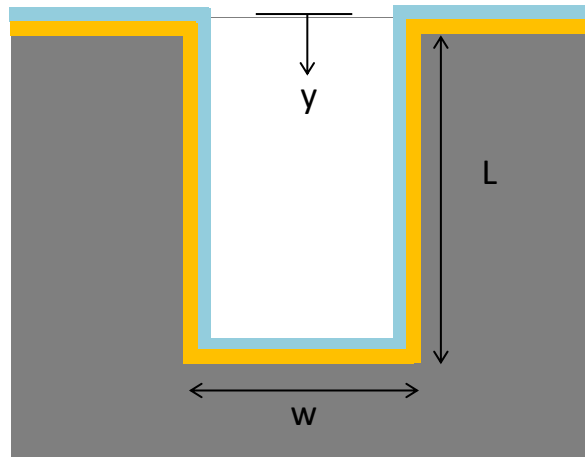


Figure 3.11. Cross section of a submicron trench.

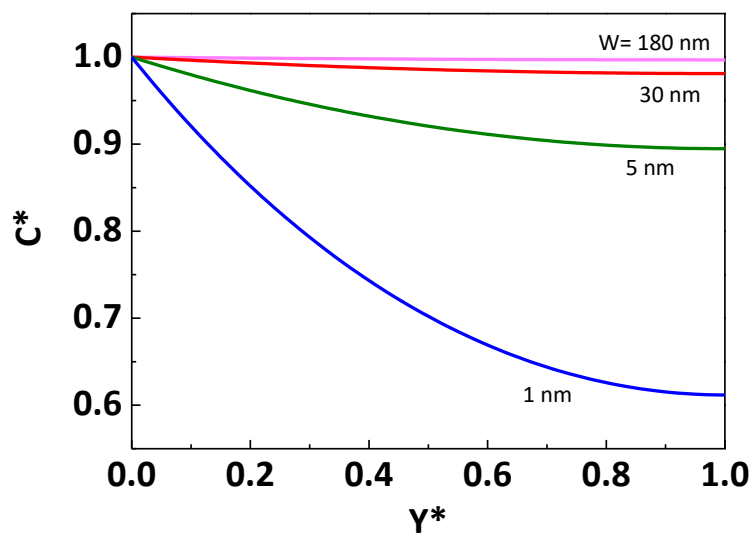


Figure 3.12. Dimensionless proton concentration vs. dimensionless distance below trench mouth.

3.2. Submicron trench filling using 2-mercaptobenzimidazole

MBI was considered as an additive capable of bottom-up filling. As shown in Table 1.1, the pK_a of MBI was far from the pH range of the typical cobalt electrodeposition solution. Therefore, there was no change in the MBI molecular form according to the pH range in this study and it was observed by UV spectra as shown in Fig. 3.13. This means that bottom-up filling is achieved with a mechanism different from that of BZI. In this study, the bottom-up filling condition using MBI was optimized and the bottom-up filling mechanism was suggested through electrochemical analysis.

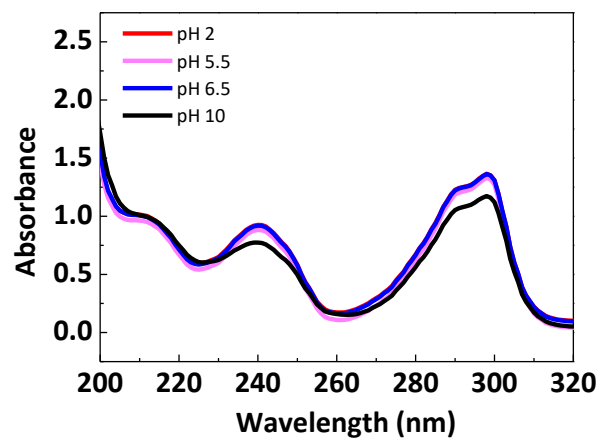


Figure 3.13. UV spectra obtained for 2-mercaptobenzimidazole at pH 2, 5.5, 6.5 and 10 at 25°C. Cobalt-free electrolyte used for UV absorbance consisted of 0.5 M H_3BO_3 and 1.0 M Na_2SO_4 . The pH was adjusted with H_2SO_4 and NaOH .

3.2.1. Optimization of Co trench filling conditions

Cobalt RDE was subjected to electrochemical analysis to investigate the effect of MBI on cobalt electrodeposition. The LSV results for the electrolyte with and without cobalt source in the presence of various concentrations of MBI are shown in Fig. 3.14. Since the standard reduction potential of protons is more positive than that of cobalt, the cobalt electrochemical experiment always involves the HER. For this reason, it is difficult to analyze the effect of additive on the HER and the cobalt deposition reaction separately. Therefore, we attempted to confirm the effect of MBI on the HER using a cobalt-free electrolyte as shown in Fig. 3.14a. Based on the results for MBI-free case, proton reduction was dominant at a relatively positive potential range of -0.4 to -0.8 V, and the current density increased because of the reduction in the number of water molecules at a potential more negative than -1.0 V, after passing the proton mass limiting region of -0.8 to -1.0 V ⁵⁷. When MBI was added, in the region where the proton reduction was dominant, the current density was maintained at a level lower than that under the MBI-free condition, indicating the suppression of proton reduction. Afterward, the breakdown of suppression occurred from approximately -0.7 V, and the

current density started to increase and became similar to that under the MBI-free condition at approximately -0.95 V. In the region where water reduction was dominant, the current was maintained lower than that under the MBI-free condition, indicating the suppression of water reduction. Interestingly, with varying the MBI concentration in the range of $50\text{--}200\text{ }\mu\text{M}$, the difference in current density was not significant. When the cobalt source was added as shown in Fig. 3.14b, the LSV results also show the breakdown of the suppression layer in two stages. As reported in a previous study, cobalt deposition begins from -0.86 V under additive-free conditions.⁷⁹ When MBI is added, as the concentration of MBI increases, the onset potential of cobalt exhibits a negative shift. In particular, at $200\text{ }\mu\text{M}$, the suppression intensity increases rapidly, and the cobalt deposition onset negatively shifts to -1.16 V. According to the results shown in Fig. 3.14a and 3.14b, MBI suppressed the HER through overall surface coverage, not the selective suppression of cobalt deposition.

The influence of MBI on submicron trench cobalt filling was examined. We attempted to determine the optimal filling condition by varying the concentration of MBI and the application potential, and the results are shown in Fig. 3.15. For the MBI-free condition, the cobalt growth proceeded conformally at the same speed at the top and bottom of the trench in the potential range of -1.0 to -1.15 V. Under the conformal

growth conditions, voids were eventually formed even though sufficient charge was applied, as shown in Fig. 3.16. At 50 μM and 100 μM MBI, where the suppression strength of MBI was relatively low, the difference in the deposition speeds at the top and bottom was not significant, resulting in a conformal filling. However, the inside of the trench was filled more than the MBI-free condition even though the same charge was applied. As shown in Fig. 3.14a, the addition of MBI suppresses the HER and increases the current efficiency of cobalt deposition, which results in more deposits inside the trench. When 150 μM was added, the suppression was strong at -1.0 V. From -1.05 V, the suppression strength began to reduce, and the bottom-up filling was achieved; however, the top was very rough and the uniformity was poor as nodes were created. At -1.1 and -1.15 V, the bottom-up filling was achieved, and the uniformity was good. At 200 μM , cobalt filling did not occur adequately because of the strong suppression effect. This coincides with the LSV results shown in Fig. 3.14b, showing a very high suppression intensity when 200 μM is added.

To electrochemically investigate the factors contributing to the difference in the trench filling, the current density change according to the potential was investigated through chronoamperometry on cobalt RDE, as shown in Fig. 3.17. When MBI was added at -1.0 V, the current density was 13 mA/cm^2 lower than that under MBI-free

condition, which implies that a strong suppression layer was formed. Contrarily, above -1.05 V, the current density relative to that of the MBI-free sample decreased to $4\text{--}6$ mA/cm^2 as the suppression layer partially broke down. From the results shown in Fig. 3.15, we can infer that the bottom-up filling occurred under the condition of weak suppression. Notably, it takes time to form the suppression layer. Comparing the initial current density between the VMS and the VMS+150 μM MBI conditions, a significant difference can be observed. For the VMS condition, when the potential was applied, a saturation point was immediately observed with a constant current density. However, when 150 μM of MBI was added, the potential was applied, and the current density decreased for approximately 10 s, as indicated by the red line in Fig. 3.17b. After that, the current profile changed according to the potential. At -1.0 V, the current density gradually decreased until approximately 50 s and saturated. Conversely, at -1.05 to -1.15 V, a partial breakdown of the suppression layer occurred, and the current density increased slightly, followed by saturation. In conclusion, the suppression layer can be formed in two steps depending on the potential, and under optimum conditions, cobalt deposition can be performed in an environment where only the first suppression layer is formed.

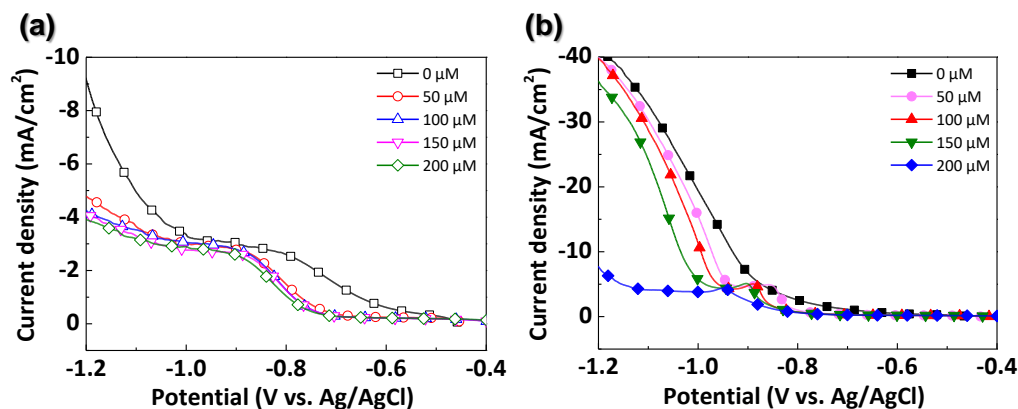


Figure 3.14. (a) Linear sweep voltammograms without cobalt source for HER. The electrolyte consisted of 0.5 M H_3BO_3 and 1.0 M Na_2SO_4 with the addition of various MBI concentrations at pH 3. (b) Linear sweep voltammograms for Co deposition in the VMS. Experimental currents are converted to current densities using the 0.071 cm^2 RDE area. The RDE was rotating at 500 rpm. Voltammetry was initiated at OCP with a 10 mV/s rate.

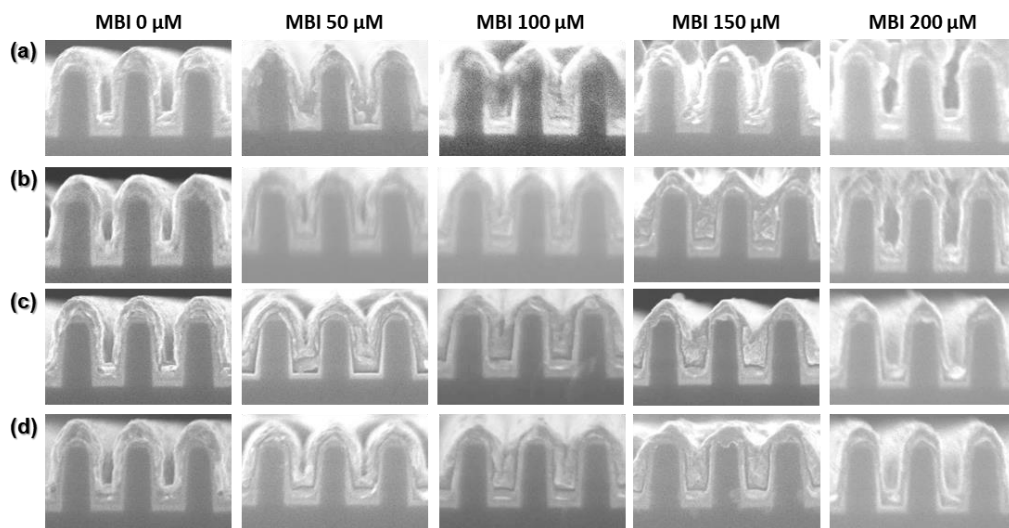


Figure 3.15. Cross sectional SEM images of 180 nm trenches deposited in the VMS with various MBI concentrations at pH 3. Deposition was performed at (a) -1.0 V, (b) -1.05 V (c) -1.1 V (d) -1.15 V vs Ag/AgCl for 300 mC/cm^2 . The patterned substrates were rotating at 500 rpm.

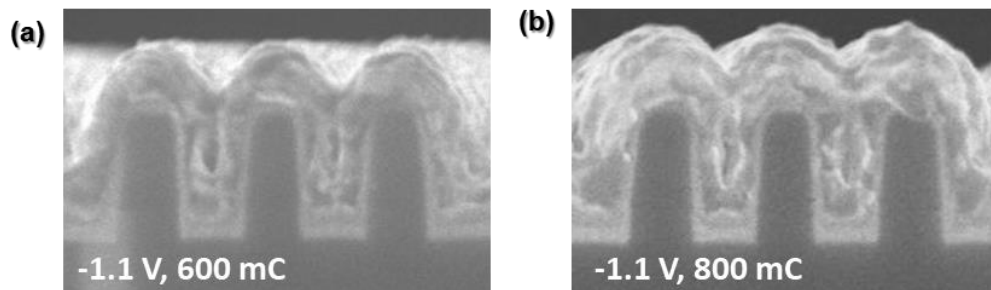


Figure 3.16. Cross sectional SEM images of 180 nm trenches deposited in the VMS without MBI at pH 3. Deposition was performed at -1.1 V vs Ag/AgCl for (a) 600 and (b) 800 mC/cm^2 . The patterned substrates were rotating at 500 rpm.

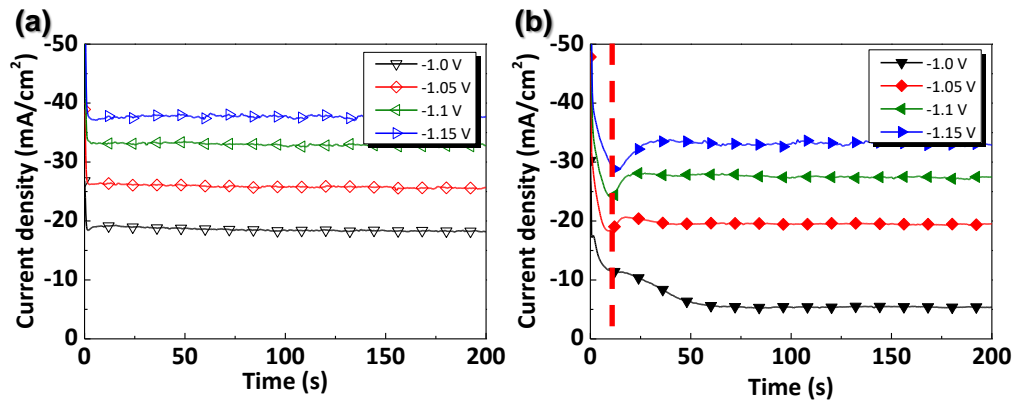


Figure 3.17. Current transients of Co deposition at (a) VMS and (b) VMS+150 μM MBI under various potentials. Experimental currents are converted to current densities using the 0.071 cm² RDE area. The RDE was rotating at 500 rpm.

3.2.2. Effect of convection intensity on suppression strength

Even though the aspect ratio (height/width) of the trench used in this study is 2, the difference in the convection intensities at the top and bottom of the submicron trench is noticeable.⁷⁷ In the trench where convection is applied, the highest convection intensity is observed at the top, and it diminishes toward the bottom. There are many studies on the bottom-up filling of copper taking advantage of the fact that this difference in convection intensity affects the suppression strength of additives.⁷⁶⁻⁷⁸ In Fig. 3.18, to determine the effect of convection on the change in the suppression effect of MBI, we performed current density comparison between the VMS and VMS+150 μM MBI at -1.1 V vs. Ag/AgCl. It was defined that the higher the current density difference, the stronger the suppression. By comparing the suppression strength through the current density difference, the largest value was observed at 500 rpm. In Fig. 3.18c, the difference between the steady-state current density values was plotted against the rotation speed. The steady-state current density was defined as the average value of the current density 25 second after applying the potential. Under the potential condition in which bottom-up filling occurred, the higher the rotation speed, the stronger the suppression, which implied that the MBI had convection-dependent adsorption. One of

the reasons for this convection dependence might be the influence of the mass transfer of MBI. As shown in Fig. 3.18b, when the rotation speed was high, the current density decreased initially and subsequently increased as the partial breakdown occurred. However, as the rotation speed decreases, the initial current profile became similar to the VMS result. That is, when the rotation speed is lowered, the supply of MBI was not sufficient, and the concentration of the MBI near the electrode substrate was considerably low, therefore, the suppression effect on cobalt deposition reduced.

By simply comparing the current, it is difficult to confirm the combined effects of the cobalt deposition and the HER suppression strength change according to the convection intensity. Thus, the difference in the deposition thickness was confirmed by electroplating the cobalt film on the bare substrate. To reduce the measurement error, the center of each sample was selected and measured by FE-SEM for 6 points. Fig. 3.19 shows the difference in film thickness according to the rotation speed under the VMS and VMS+150 μM MBI conditions. When cobalt film electrodeposition was conducted with the same charge, it was established that the higher the rotation speed, the higher the thickness under the VMS condition. This is because when the rotation speed is high, the deposition is performed at a high current density, owing to the effect of the sufficient mass transfer of Co^{2+} and protons, and the current efficiency increases

at a high current density, owing to the characteristics of cobalt electrodeposition.²⁶ For the VMS+150 μ M MBI condition, despite exhibiting the highest current density at 500 rpm, the thickness was the lowest, and the thickness increased as the rotation speed decreased. When the rotation speed was lowered, the mass transfer of MBI was retarded, and the concentration of MBI at the electrode surface decreased. As can be observed from the LSV results in Fig. 3.14, the suppression effect of the HER was maintained even at relatively low MBI concentrations. However, the suppression strength of cobalt deposition depended on the MBI concentration. In other words, the suppression of HER was maintained at low concentrations of MBI to maintain a high current efficiency; however, the cobalt suppression strength rapidly reduced, resulting in a relatively high deposition rate. Conversely, at 500 rpm, the MBI supply was sufficient because of the strong convection, and the cobalt film thickness was decreased by the relatively strong suppression of cobalt deposition to offset the effect of increasing the current efficiency by suppressing hydrogen evolution. In a patterned surface, such as a trench, the consumption of MBI would be more concentrated at the top than at the bottom, and the difference in concentration of MBI would be higher than that in the planar surface, which was only affected by the rotation speed variance to afford the mass-transfer difference. When deposition was performed with 50 μ M

MBI and 50 rpm by simulating the bottom conditions, the Co film thickness was much higher than with 150 μ M MBI and 500 rpm which simulating the top conditions as shown in Fig. 3.20.

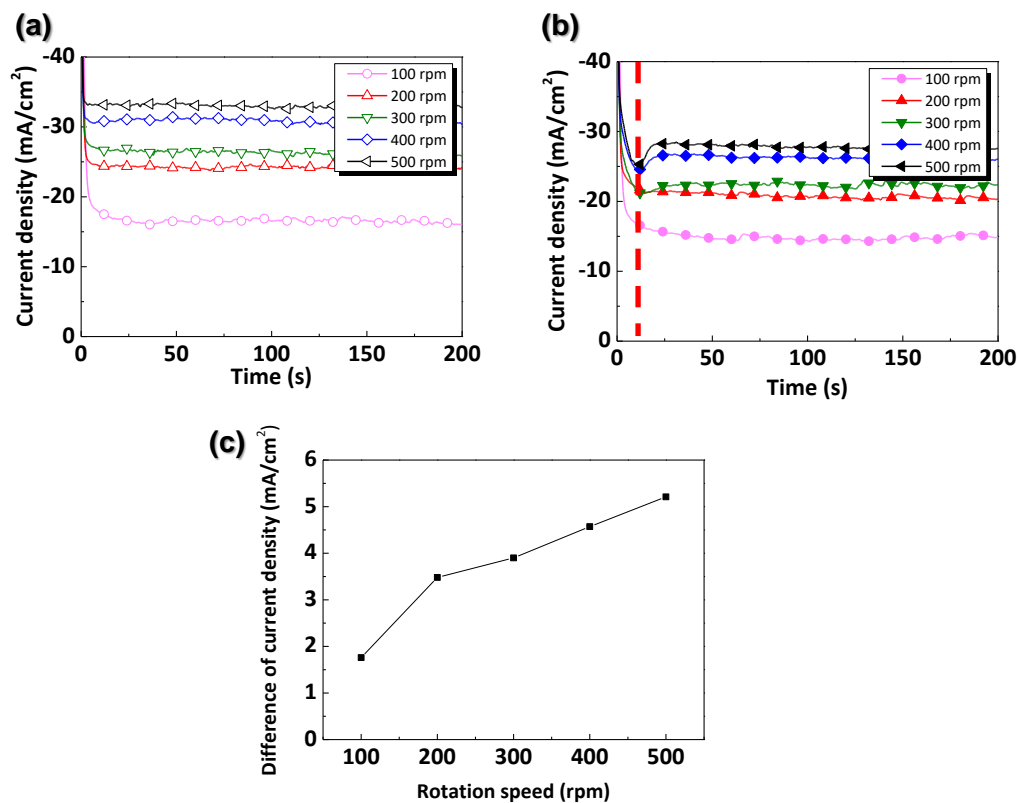


Figure 3.18. Effect of rotation speed on the chronoamperometry for Co deposition at (a) VMS and (b) VMS+150 μM MBI. (c) Difference between the steady-state current density as a function of rotation speed. The base electrolyte consists of 0.1 M $\text{CoSO}_4 \cdot 7\text{H}_2\text{O}$, 0.5 M H_3BO_3 and 1.0 M Na_2SO_4 with pH 3. Chronoamperometry was performed at -1.1 V vs Ag/AgCl. Experimental currents are converted to current densities using the 0.071 cm^2 RDE area.

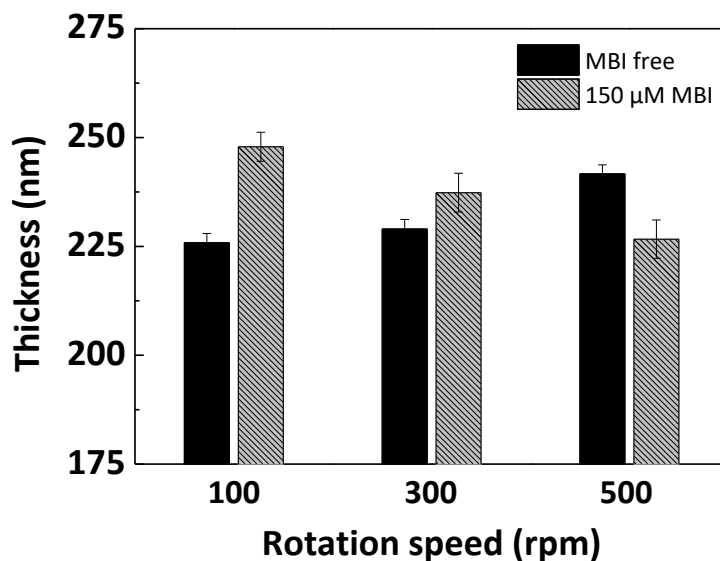


Figure 3.19. Comparison of Co film thickness as a function of rotation speed at MBI free and 150 μM MBI. The base electrolyte consists of 0.1 M $\text{CoSO}_4 \cdot 7\text{H}_2\text{O}$, 0.5 M H_3BO_3 and 1.0 M Na_2SO_4 with pH 3. The deposition was performed on the PVD Co wafer at -1.1 V vs Ag/AgCl for 1.0 C/cm^2 . The Co film thickness was measured by FE-SEM after cross section.

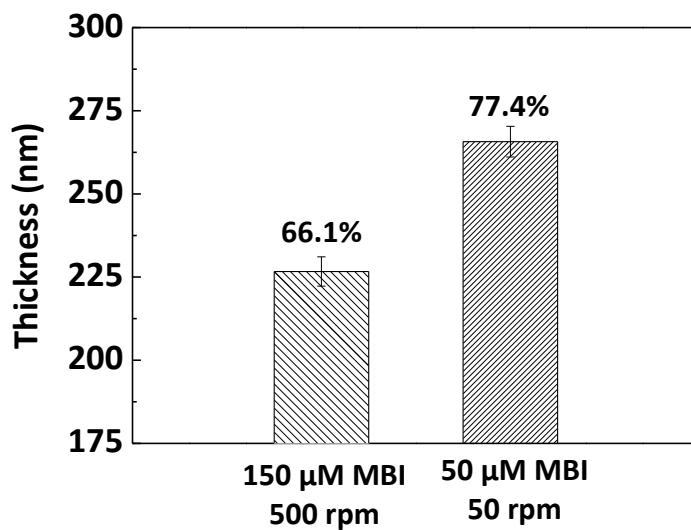


Figure 3.20. Comparison of cobalt film thickness simulating the conditions of top (150 μM MBI, 500 rpm) vs. bottom (50 μM MBI, 50 rpm). The base electrolyte consists of 0.1 M $\text{CoSO}_4 \cdot 7\text{H}_2\text{O}$, 0.5 M H_3BO_3 and 1.0 M Na_2SO_4 with pH 3. The deposition was performed on the PVD Co wafer at -1.1 V vs Ag/AgCl for 1.0 C/cm^2 . The cobalt film thickness was measured by FE-SEM after cross section.

3.2.3. Filling mechanism of 2-mercaptobenzimidazole

The filling profile according to the applied charge is shown in Fig. 3.21. When the filling is initiated by applying a potential, the concentrations of all the solution species including MBI are equal to the base solution composition at the top and bottom of the trench. Therefore, the cobalt growth proceeds conformally without any difference in the deposition speed at the top and bottom. This was demonstrated with the image obtained at 100 mC/cm^2 where the initial stage of cobalt filling occurred. From 150 mC/cm^2 , a V-shape profile was formed as the deposition was enhanced at the bottom corner. The beginning of V-shape profile coincides with the start of steady-state current in chronoamperometry shown in Fig. 3.22. Deposition speed of the bottom reaches at steady-state current density between 5 and 7.5 second, earlier than that showed in planar geometry (Fig. 3.17). As the deposition progresses, the mass transport on the bottom of the trench is expected to be significantly less than that on the top. The MBI concentration gradients quickly develop within the trench because of the relatively slow diffusion of MBI. Therefore, at the top where the concentration of MBI is sufficient, the suppression of cobalt deposition by MBI is strong. At the bottom where

the concentration of MBI is relatively low, the suppression of cobalt deposition is low, while the suppression of HER remains strong, resulting in a high current efficiency. In conclusion, the proximity to the bottom has a linear relationship with the ease of deposition. Therefore, the inner V-shape profile was maintained; however, the notch angle gradually increased as the filling proceeded, enabling the bottom-up filling profile to become almost flat at the end as shown at 400 mC/cm^2 . The concentration of MBI by location and its effect on cobalt deposition are depicted in Fig. 3.23.

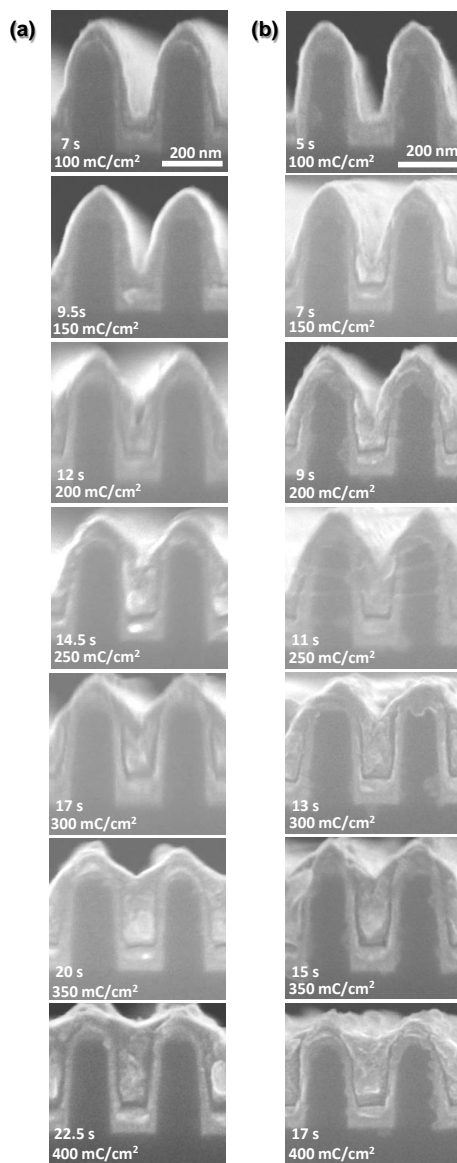


Figure 3.21. The evolution of cobalt feature filling obtained at (a) -1.1 V and (b) -1.15 V in an electrolyte consisting of 0.1 M $\text{CoSO}_4 \cdot 7\text{H}_2\text{O}$, 0.5 M H_3BO_3 and 1.0 M Na_2SO_4 with 150 μM MBI at pH 3. The patterned substrates were rotating at 500 rpm.

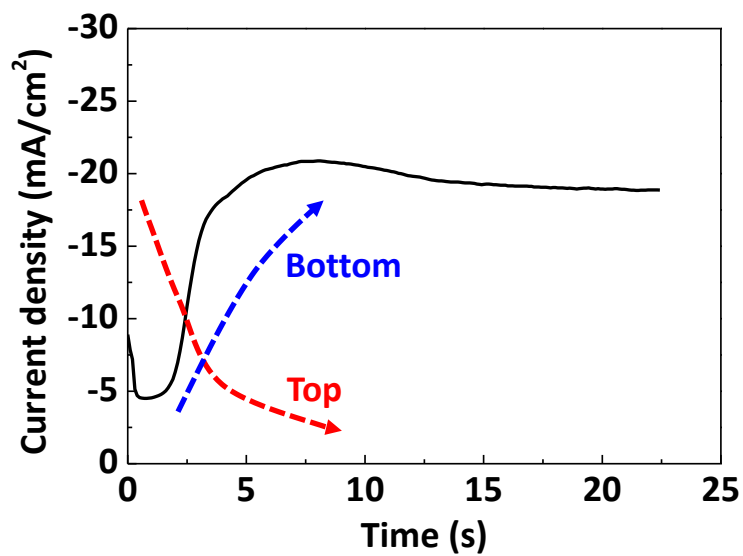


Figure 3.22. The current transients curve during the trench-filling in the VMS with 150 μM of MBI at pH 3. Deposition was performed at -1.1 V vs Ag/AgCl for 400 mC/cm^2 . The patterned substrates were rotating at 500 rpm.

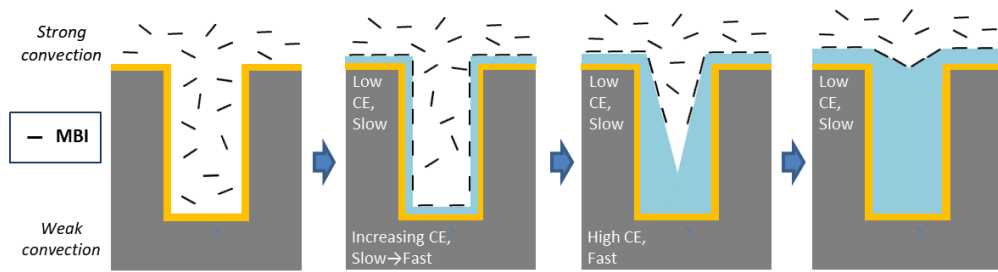


Figure 3.23. Proposed MBI working mechanism for void-free cobalt fill under 500 rpm convection system. CE = current efficiency.

CHAPTER IV

Conclusion

In this study, two types of suppressors, which have relation with the HER were introduced for cobalt superfilling of submicron trench. At first, benzimidazole (BZI) whose suppression behavior changes according to the change in pH of the electrode surface is presented by considering the pH of the cobalt deposition solution and pK_a value of the additive. It was demonstrated that void-free filling can be performed even in a trench with a low aspect ratio. BZI exists in a protonated form when it is in a solution with a pH lower than its pK_a value and has a cobalt suppression effect. However, as the pH increased, the proportion of neutral form also increased, and the suppression effect was weakened, suggesting that it is sensitive to the proton concentration on the electrode surface. Since the cobalt deposition reaction is accompanied by hydrogen reduction, the pH of the electrode surface changes when the proton supply is changed by adjusting the rotation rate. A strong suppression layer is formed at a rotation rate of 400 rpm or higher, but when the pH of the electrode surface increases because of the low rotation rate, the suppression effect of BZI is significantly

reduced. This is applicable to feature filling where the convection strength at the top and bottom is different due to topographical characteristics. As a result of performing the actual trench filling, the convection strength difference cannot be induced initially owing to the low aspect ratio, resulting in conformal deposition. However, as the deposition progresses, the aspect ratio of the inside trench becomes higher, and eventually void-free filling is performed. Based on these results, it may be possible to use other organic additives, which have a pK_a value higher than the pH of the deposition solution, and the suppression behavior changes according to how the molecular form changes.

In addition, 2-mercaptobenzimidazole (MBI) as a suppressor for submicron trench filling was also investigated. The addition of MBI to a cobalt electrodeposition electrolyte suppressed both the cobalt deposition and the HER. The cobalt suppression effect varied significantly with the MBI concentration, while the HER suppression effect did not. Superconformal filling of submicron trenches was achieved by cobalt electrodeposition with 150 μM of MBI at -1.1 and -1.15 V vs. Ag/AgCl. The formation and behavior of the MBI suppression layer were strongly influenced by the potential. The MBI suppression layer was formed in approximately 10 s after applying the potential, and it was divided into two cases: one where a partial breakdown

occurred, and the other where a relatively strong suppression layer was formed depending on the potential. Cobalt bottom-up filling was possible in the potential region where the partial breakdown occurred. In addition, the intensity of the suppression of MBI for cobalt deposition varied according to convection intensity; this is attributable to the concentration difference because of the mass transfer of MBI. At the top where strong convection was maintained, the MBI suppression effect on cobalt deposition was dominant because of the sufficient supply of MBI. However, the convection intensity decreased as it entered the trench, resulting in an MBI concentration gradient. Furthermore, the suppression effect on cobalt deposition was considerably weak at the bottom, while the effect of increasing the current efficiency by suppressing the HER was maintained, enabling the bottom-up filling with a V-shape profile. Through this, we investigated the reason for the occurrence of superconformal cobalt filling, even with the addition of a single additive that exerts only a suppression effect.

In fact, cobalt filling is meaningful in patterns below 10 nm. In this study, the mechanism of action of each additive was revealed using a submicron trench, but it is based on the diffusion-adsorption-consumption model of additives and protons, so if the aspect ratio is maintained above a certain level, it will be applicable even if the

width of the feature is narrowed. It is a subject for future study to perform cobalt filling using additives in a 10 nm scale trench.

References

1. IRDS, *International Roadmap for Devices and Systems* (2018).
2. Intel's e-DRAM Shows up in the Wild, in, p.
<http://chipworksrealchips.blogspot.com/2014/02/intels>, Chipworks.com (2014).
3. J. S. Chawla, F. Gstrein, K. P. O'Brien, J. S. Clarke and D. Gall, *Phys Rev B*, **84** (2011).
4. D. Choi and K. Barmak, *Electron Mater Lett*, **13**, 449 (2017).
5. D. Josell, S. H. Brongersma and Z. Tokei, *Annu Rev Mater Res*, **39**, 231 (2009).
6. T. Sun, B. Yao, A. P. Warren, K. Barmak, M. F. Toney, R. E. Peale and K. R. Coffey, *Phys Rev B*, **79** (2009).
7. T. Sun, B. Yao, A. P. Warren, K. Barmak, M. F. Toney, R. E. Peale and K. R. Coffey, *Phys Rev B*, **81** (2010).
8. W. Zhang, S. H. Brongersma, O. Richard, B. Brijs, R. Palmans, L. Froyen and K. Maex, *Microelectron Eng*, **76**, 146 (2004).
9. *IEEE, International Electron devices Meeting* (2017).
10. R. L. Graham, G. B. Alers, T. Mountsier, N. Shamma, S. Dhuey, S. Cabrini, R.

- H. Geiss, D. T. Read and S. Peddeti, *Appl Phys Lett*, **96** (2010).
11. D. Choi, *Korean J Met Mater*, **56**, 605 (2018).
 12. M. R. Baklanov, C. Adelmann, L. Zhao and S. De Gendt, *Ecs J Solid State Sc*, **4**, Y1 (2015).
 13. K. Sankaran, S. Clima, M. Mees and G. Pourtois, *Ecs J Solid State Sc*, **4**, N3127 (2015).
 14. D. Gall, *J Appl Phys*, **119**, 085101 (2016).
 15. H. Dixit, A. Konar, R. Pandey and T. Ethirajan, *J Phys D Appl Phys*, **50**, 455103 (2017).
 16. R. N. Akolkar, F. Gstrein and D. J. Zierath, Pat. US20120153483A1, in (2012).
 17. N. Bekiaris, Z. Wu, H. Ren, M. Naik, J. H. Park, M. Lee, T. H. Ha, W. Hou, J. R. Bakke, M. Gage, Y. Wang and J. Tang, in *2017 IEEE International Interconnect Technology Conference (IITC)*, p. 1 (2017).
 18. F. Griggio, J. Palmer, F. Pan, N. Toledo, A. Schmitz, I. Tsameret, R. Kasim, G. Leatherman, J. Hicks, A. Madhavan, J. Shin, J. Steigerwald, A. Yeoh and C. Auth, *2018 IEEE International Reliability Physics Symposium (IRPS)*, 6E.3 (2018).
 19. R. Grover, T. Acosta, C. AnDyke, E. Armagan, C. Auth, S. Chugh, K. Downes,

- M. Hattendorf, N. Jack, S. Joshi, R. Kasim, G. Leatherman, S. Lee, C. Lin, A. Madhavan, H. Mao, A. Lowrie, G. Martin, G. McPherson, P. Nayak, A. Neale, D. Nminibapiel, B. Orr, J. Palmer, C. Pelto, S. S. Poon, I. Post, T. Pramanik, A. Rahman, S. Ramey, N. Seifert, K. Sethi, A. Schmitz, H. Wu and A. Yeoh, in *2020 IEEE International Reliability Physics Symposium (IRPS)*, p. 1 (2020).
20. C. J. Jezewski, J. S. Clarke, T. K. Indukuri, F. Gstrein and D. J. Zierath, Pat. US9514983B2, in (2016).
21. F. W. Mont, X. Zhang, W. Wang, J. J. Kelly, T. E. Standaert, R. Quon and E. T. Ryan, in *2017 IEEE International Interconnect Technology Conference (IITC)*, p. 1 (2017).
22. A. Yeoh, A. Madhavan, N. Kybert, S. Anand, J. Shin, M. Asoro, S. Samarajeewa, J. Steigerwald, C. Ganpule, M. Buehler, A. Tripathi, V. Souw, M. Haran, S. Nigam, V. Chikarmane, P. Yashar, T. Mulé, Y. Wu, K. Lee, M. Aykol, K. Marla, P. Sinha, S. Kirby, H. Hiramatsu, W. Han, M. Mori, M. Sharma, H. Jeedigunta, M. Sprinkle, C. Pelto, M. Tanniru, G. Leatherman, K. Fischer, I. Post and C. Auth, in *2018 IEEE International Interconnect Technology Conference (IITC)*, p. 144 (2018).
23. J. Zheng, P. Chen, T. H. Baum, R. R. Lieten, W. Hunks, S. Lippy, A. Frye, W. Li, J. O. Neill, J. Xu, J. Zhu, J. Bao, V. Machkaoutsan, M. Badaroglu, G. Yeap, G.

Murdoch, J. Bömmels and Z. Tökei, in *2015 IEEE International Interconnect Technology Conference and 2015 IEEE Materials for Advanced Metallization Conference (IITC/MAM)*, p. 265 (2015).

24. D. Josell, M. Silva and T. P. Moffat, *J Electrochem Soc*, **163**, D809 (2016).

25. C. H. Lee, J. E. Bonevich, J. E. Davies and T. P. Moffat, *J Electrochem Soc*, **156**, D301 (2009).

26. M. A. Rigsby, L. J. Brogan, N. V. Doubina, Y. H. Liu, E. C. Opocensky, T. A. Spurlin, J. Zhou and J. D. Reid, *J Electrochem Soc*, **166**, D3167 (2018).

27. J. Wu, F. Wafula, S. Branagan, H. Suzuki and J. van Eisdien, *J Electrochem Soc*, **166**, D3136 (2018).

28. D. R. Gabe, *J Appl Electrochem*, **27**, 908 (1997).

29. N. Pradhan, T. Subbaiah, S. C. Das and U. N. Dash, *J Appl Electrochem*, **27**, 713 (1997).

30. M. A. Rigsby, T. A. Spurlin and J. D. Reid, *J Electrochem Soc*, **167** (2020).

31. Y. Tsuru, M. Nomura and F. R. Foulkes, *J Appl Electrochem*, **32**, 629 (2002).

32. R. Sard, C. D. Schwartz and R. Weil, *J Electrochem Soc*, **113**, 424 (1966).

33. B. Tripathy, P. Singh and D. Muir, *Metallurgical and Materials Transactions B*, **32**, 395 (2001).

34. S. Ali and M. Salim, *Asian J Chem*, **25**, 4137 (2013).
35. J. S. Santos, R. Matos, F. Trivinho-Strixino and E. C. Pereira, *Electrochim Acta*, **53**, 644 (2007).
36. W. A. Badawy, F. M. Al-Kharafi and J. R. Al-Ajmi, *J Appl Electrochem*, **30**, 693 (2000).
37. Y. Yu, Z. Song, H. Ge, G. Wei and L. Jiang, *Materials Research Innovations*, **20**, 280 (2016).
38. A. Vincenzo and P. L. Cavallotti, *Electrochim Acta*, **49**, 4079 (2004).
39. J. S. Santos, F. Trivinho-Strixino and E. C. Pereira, *Surf Coat Tech*, **205**, 2585 (2010).
40. J. T. Matsushima, E. Trivinho-Strixino and E. C. Pereira, *Electrochim Acta*, **51**, 1960 (2006).
41. T. Cohen-Hyams, W. D. Kaplan and J. Yahalom, *Electrochem Solid St*, **5**, C75 (2002).
42. M. Li, Z. W. Wang and R. G. Reddy, *Electrochim Acta*, **123**, 325 (2014).
43. R. Sekar, *T I Met Finish*, **93**, 44 (2015).
44. R. F. Renner and K. C. Liddell, *J Appl Electrochem*, **32**, 621 (2002).
45. Y. Liu, Z. J. Li, Y. C. Wang and W. Wang, *T Nonferr Metal Soc*, **24**, 876

(2014).

46. P. Patnaik, S. K. Padhy, B. C. Tripathy, I. N. Bhattacharya and R. K. Paramguru, *T Nonferr Metal Soc*, **25**, 2047 (2015).

47. O. E. Kongstein, G. M. Haarberg and J. Thonstad, *J Appl Electrochem*, **37**, 669 (2007).

48. A. E. Elsherief, *J Appl Electrochem*, **33**, 43 (2003).

49. D. Josell, D. Wheeler, W. H. Huber and T. P. Moffat, *Phys Rev Lett*, **87** (2001).

50. M. H. Lee, Y. Lee, M. Sung, S. K. Cho, Y. G. Kim and J. J. Kim, *J Electrochem Soc*, **167** (2020).

51. T. P. Moffat, J. E. Bonevich, W. H. Huber, A. Stanishevsky, D. R. Kelly, G. R. Stafford and D. Josell, *J Electrochem Soc*, **147**, 4524 (2000).

52. T. P. Moffat, D. Wheeler, W. H. Huber and D. Josell, *Electrochem Solid St*, **4**, C26 (2001).

53. M. Sung, S. H. Kim, H. J. Lee, T. Lim and J. J. Kim, *Electrochim Acta*, **295**, 224 (2019).

54. M. Sung, Y. Yoon, J. Hong, M. J. Kim and J. J. Kim, *J Electrochem Soc*, **166**, D546 (2019).

55. Q. Huang, T. W. Lyons and W. D. Sides, *J Electrochem Soc*, **163**, D715 (2016).

56. O. E. Kongstein, G. M. Haarberg and J. Thonstad, *J Electrochem Soc*, **157**, D335 (2010).
57. V. Grozovski, S. Vesztergom, G. G. Lang and P. Broekmann, *J Electrochem Soc*, **164**, E3171 (2017).
58. A. Franczak, F. Bohr, A. Levesque and J. Chopart, *Research & Reviews: Journal of Chemistry*, **4**, 74 (2015).
59. M. A. Rigsby, L. J. Brogan, N. V. Doubina, Y. Liu, E. C. Opocensky, T. A. Spurlin, J. Zhou and J. D. Reid, *ECS Transactions*, **80**, 767 (2017).
60. J. Aljourani, K. Raeissi and M. A. Golozar, *Corros Sci*, **51**, 1836 (2009).
61. M. Amini, M. Aliofkhazraei, A. H. N. Kashani and A. S. Rouhaghdam, *Int J Electrochem Sc*, **12**, 8708 (2017).
62. F. Lallemand, L. Ricq, E. Deschaseaux, L. De Vettor and P. Bercot, *Surf Coat Tech*, **197**, 10 (2005).
63. F. Lallemand, L. Ricq, A. Wery, P. Bercot and J. Pagetti, *Appl Surf Sci*, **228**, 326 (2004).
64. C. H. Lee, J. E. Bonevich, U. Bertocci, K. L. Steffens and T. P. Moffat, *J Electrochem Soc*, **158**, D366 (2011).
65. D. H. Taffa, I. Hamm, C. Dunkel, I. Sinev, D. Bahnemann and M. Wark, *Rsc*

Adv, **5**, 103512 (2015).

66. T. M. Braun, S. H. Kim, H. J. Lee, T. P. Moffat and D. Josell, *J Electrochem Soc*, **165**, D291 (2018).

67. D. Josell and T. P. Moffat, *J Electrochem Soc*, **163**, D322 (2016).

68. S. K. Kim, J. E. Bonevich, D. Josell and T. P. Moffat, *J Electrochem Soc*, **154**, D443 (2007).

69. C. H. Lee, J. E. Bonevich, J. E. Davies and T. P. Moffat, *J Electrochem Soc*, **155**, D499 (2008).

70. C. H. Lee and T. P. Moffat, *Electrochim Acta*, **55**, 8527 (2010).

71. H. S. Lu, X. Zeng, J. X. Wang, F. Chen and X. P. Qu, *J Electrochem Soc*, **159**, C383 (2012).

72. M. A. Rigsby, T. A. Spurlin and J. D. Reid, *J Electrochem Soc*, **167**, 112507 (2020).

73. H. Z. Cao, L. L. Hu, H. B. Zhang, G. Y. Hou, Y. P. Tang and G. Q. Zheng, *Int J Electrochem Sc*, **15**, 6769 (2020).

74. G. Jerez, G. Kaufman, M. Prystai, S. Schenkeveld and K. K. Donkor, *Journal of separation science*, **32**, 1087 (2009).

75. G. Jerez, G. Kaufman, M. Prystai, S. Schenkeveld and K. K. Donkor, *J Sep*

Sci, **32**, 1087 (2009).

76. K. G. Jordan and C. W. Tobias, *J Electrochem Soc*, **138**, 1933 (1991).

77. U. Landau, E. Malyshev, R. Akolkar and S. Chivilikhin, in (2003).

78. K. M. Takahashi and M. E. Gross, *J Electrochem Soc*, **146**, 4499 (1999).

79. J. Kang, M. Sung, J. Byun, O. J. Kwon and J. J. Kim, *J Electrochem Soc*, **167**
(2020).

국문 초록

코발트는 구리 회로를 대체 할 가장 유망한 재료 중 하나이다. 본 연구에서는 벤젠 고리와 이미다졸 기반의 단일 첨가제를 억제제로 사용하여 서브마이크론 트렌치를 결함 없이 성공적으로 채웠고 그 충전 메커니즘을 연구하였다. 코발트 전착은 수소 발생 반응(HER)을 포함하며, 패턴 채움에서 지형적 특성으로 인해 수소 이온 공급이 위치에 따라 달라져 pH 및 수소 흡착과 같은 전극 표면 변화를 초래한다. 이 현상을 바탕으로 pH에 따라 억제 효과가 다른 벤지이미다졸(BZI)을 첨가제로 사용하여 결함 없는 트렌치 충진을 달성하였다. 먼저 선형주사전위법 실험을 통해 pH에 따른 첨가제의 억제 거동 변화를 확인하였다. 다음으로 실제 코발트 도금이 억제되는 전위 영역을 확인하기 위해 고정된 BZI 농도에서 시간대전류법을 수행하였다. BZI의 억제 효과에 대한 전극 근처의 수소 이온 농도의 효과를 입증하기 위해 다양한 회전 속도를 사용한 시간대전류 분석도 수행되었다. 마지막으로 BZI를 사용하는 낮은 중황비 트렌치에서의 결점 없는 충전 작업 메커니즘이 제안되었다. 본 연구에서는 코발트 도금 용액의 pH와 첨가제의 pK_a

값을 고려하여 전극 표면의 pH 변화에 따라 억제 거동이 변화하는 단일 첨가제를 제안하였다. 또한, 충전 공정 중 트렌치 내부에서의 수소 이온 분포 변화를 계산하여 중황비가 낮은 트렌치에서도 결함이 없는 충전이 가능함을 입증하였다.

우리는 또한 코발트 도금과 HER를 모두 억제하는 2-머캅토벤지이미다졸(MBI)을 추가하였을 때 서브마이크론 트렌치의 초등각 코발트 충진을 연구하였다. 이 단일 첨가제가 초등각 코발트 충진을 가능하게 하는 메커니즘을 조사하였다. 억제 층의 형성과 파괴는 선형주사전위법과 시간대전류법을 통해 파악하였다. 대류에 의한 MBI의 국소 농도 차이는 코발트 환원 및 HER에 대해 다른 억제 효과를 발휘하여 코발트의 도금 속도와 전류 효율을 변화시켰다. 이러한 현상은 서브마이크론 트렌치의 상단과 하단 사이에 증착 속도 차이를 유발하여 V 자형 프로파일로 상향식 코발트 충진을 가능하게 하였다. 본 연구에서 우리는 이전에 몇 가지밖에 소개되지 않은 코발트 패턴 충진을 위한 새로운 첨가제를 도입하고 HER 관련 관점에서 각 충전 메커니즘을 설명하였다.

주요어: 서브마이크론 트렌치, 코발트, 전해도금, 단일 첨가제 조성, 수퍼필링,
수소 발생 반응

학 번: 2017-38822